Stability enhancement and chatter suppression in continuous radial immersion milling

Dongqian Wang*[1,2], Lars Penter[1,2], Albrecht Hänel[2], Steffen Ihlenfeldt[1,2], Marian Wiercigroch[3]

E-mail address: dongqian.wang@tu-dresden.de

[1]Institute of Mechatronic Engineering, Dresden University of Technology, 01069 Dresden, Germany

[2]Fraunhofer Institute for Machine Tools and Forming Technology IWU, 09126 Chemnitz, Germany

[3]Centre for Applied Dynamic Research, School of Engineering, University of Aberdeen, Scotland, UK

Abstract: For continuous radial immersion milling operations, the dominant mode shape becomes difficult to determine when stiffness of the tool and workpiece are comparable, and this can pose a great challenge for ensuring machining processes stability. In this paper, we propose a rapid method to obtain time-varying modal parameters of the workpiece by combining experimental measurements with the receptance coupling method. Firstly, the contact parameters between the workpiece and vise were identified by a so-called dynamic coupling matrix. Then the mode shapes and the time-varying natural frequency of the workpiece were determined using the modal parameters of workpiece. Finally, the stability lobe diagrams (SLDs) were computed using the modal parameters and then were validated by undertaking immersion milling experiments. The experiments showed a more conservative and practical SLD for general workpiece under continuous radial immersion, where the workpiece mode had not always dominated the machining process. Based on the proposed method, we also explored two modifications in form of additional cylinder masses and passive support, to suppress chatter. Both modifications were effective in enhancing the minimum boundary of the conservative SLD, and the modification of passive support worked better. Although the modification of the workpiece could improve the stability boundary, it indirectly affected the dynamics of the milling tool through the interaction area between the workpiece and milling tool.

Keywords: Continuous immersion milling, Receptance coupling, Stability lobe diagram, Chatter suppression

Nomenclature

R_{uv}	Generalized receptance matrix, v - excitation location, u - response location	K_{tc}, K_{nc}	Cutting force coefficients in tangential and normal direction (N/mm²)
$H_{uv} = \dfrac{x_u}{f_v}$	Displacement-force receptance	$\mathbf{F}_t(t)$, $\mathbf{F}_w(t)$	Force acting on the milling tool, force acting on the workpiece (N)
$L_{uv} = \dfrac{x_u}{\chi_v}$	Displacement coupling receptance	$g(\theta_j)$	Heaviside's step function
$N_{uv} = \dfrac{\alpha_u}{f_v}$	Rotation angle-force receptance	θ_{en}, θ_{ex}	Entry angle, exit angle (°)
$P_{uv} = \dfrac{\alpha_u}{\chi_v}$	Rotation angle coupling receptance	$\mathbf{q}_w(\omega)$	Workpiece dynamic displacement in frequency domain
G_{11}	Assembly receptance matrix at the top of the workpiece	$\mathbf{F}_w(\omega)$	Force acting on the workpiece in frequency domain
R_{uv}^A, R_{uv}^B, R_{uv}^C	Generalized receptance matrices of Substructure A, Substructure B and Assembly C	$\mathbf{\Phi}_t$, $\mathbf{\Phi}_w$	Mass-normalized mode shape matrix of the milling tool and workpiece respectively
G_{22}	Assembly receptance matrix at the top of the substructure B	n_t, n_w	Number of excited modes of milling tool and workpiece respectively
K	Dynamic coupling matrix	ζ_r	Damping ratio of the rth mode
j	Ordinal number of cutter tooth	β	Helix angle (°)
s	Number of the discretization slice	$\mathbf{q}_t(t)$, $\mathbf{q}_w(t)$	Tool dynamic displacement, workpiece dynamic displacement
$h_j(t)$	Instantaneous uncut chip thickness of jth tooth	$\mathbf{\Phi}_{wu}$	Updated mode shape matrix of the workpiece
f_t	Feed per tooth (mm/Z)	$\mathbf{\Phi}_{w,s}$	Mode shape of the sth row
θ_j	Instantaneous angular position for the jth tooth (°)	ω_r	Natural frequency of the rth mode (rad/s)
N	Number of cutting teeth	$\mathbf{K}$	Stiffness matrix
Ω	Spindle speed (rpm)	$\mathbf{M}$	Mass matrix
d	Diameter of milling tool (mm)	$\mathbf{C}$	Damping matrix
τ	Time delay	FRF_{exp}	Experimental FRF
N	Number of cutter teeth	FRF_{sim}	Simulated FRF
$\mathbf{H_0(\omega)}$	FRF of the original structure	$\mathbf{H_u(\omega)}$	FRF of the modified structure
$\mathbf{q_0(\omega)}$	Response displacement of the original structure	$\mathbf{q_u(\omega)}$	Response displacement of the modified structure

1. Introduction

Stability lobe diagrams (SLDs) are important characteristics in selecting of machining process parameters and ultimately ensuring required geometrical and surface finish accuracies, see for example [1,2]. In fact, SLD boundaries are neither static nor constant but vary dynamically, and this must be considered when predicting machining process stability. This variation is mainly caused by complex process interactions, speed-dependent effects, time-varying modal parameters and uncertainties. A wide variety of SLDs can be found in literature examining influences on complicated process interactions, such as process damping [3,4], runouts [5], cross responses [6,7], force-induced deformations [8], tool orientations [9], dominant modes [10], state dependent effects [11], unstable islands [12,13] and other effects. These studies have extended a suite of machining dynamics models and have demonstrated complex dynamic interactions between a machine tool and workpiece.

When a spindle is rotating, its speed change can also have a significant effect on the dynamics of milling processes. Grossi *et al.* [14,15] investigated a variation of cutting force coefficients and frequency response function (FRF) at the tool point for different spindle speeds and established the relationships between cutting force coefficients and a spindle speed as well as for the tool point FRF and a spindle speed. A variation of spindle speed also introduces nonlinear factors such as gyroscopic effects and a process damping. Wan *et al.* [16] analyzed the gyroscopic effect and incorporated it into the stability analysis at high spindle speeds. Molnar *et al.* [17] constructed a velocity-dependent process-damping model to explain the reasons behind low-speed stability improvements in radial immersion milling. In addition to alterations of modal parameters at the tool point due to speed, the change of modal parameters of the workpiece due to the removed material is the main source of time-varying modal parameters. Both these effects pose a great challenge for an accurate prediction of SLDs. With regards to uncertainties, Zhang *et al.* [18] considered an uncertainty of spindle-tool system and developed the SLDs for the lower and upper bounds, showing how machining parameters can exhibit uncertainty within those two bounds. Löser *et al.* [19] investigated uncertain parameters in milling processes and constructed an efficient computational model for the stability assessment. From the uncertainty point of view, there are standard deviations above and below the mean stability limit, so that the stability boundary varies within this range. However, sources of uncertainty are diverse, and it is unrealistic to consider various influencing factors in SLD construction during practical machining process. As the result, uncertainty regions have been used to explain the SLD considering certain influencing factors, but there is no established view so far.

For the machining system, investigations of time-varying modal parameters have been focused on thin-walled workpiece because typically it has a low stiffness when compared to the tool [20]. At present, determination of time-varying modal parameters of a workpiece relies on empirical modal analysis, finite element method and structural dynamics predictions [21-23]. As pointed out earlier, Sun and Jiang [8] proposed an iterative strategy to determine the force-induced deformation with the corresponding engagement boundary, and they modified both the static and dynamic stiffness at each tool feed position to obtain the time-varying modal parameters. Song *et al.* [24] obtained the instantaneous dynamic characteristics of thin-walled workpiece by means of iterative formulas. Tuysuz and Altintas [25,26] investigated the dynamic characteristics of thin-walled workpiece using the substructure reduction method for both frequency and time domains. Hamann and Eberhard [27] showed a parametric order reduction method to capture time-varying dynamics of the workpiece and derived the SLD. In order to reduce time to obtain the in-process dynamics of thin-walled workpiece, Dang *et al.* [28] proposed a stability prediction method, which reduces a number of degrees-of-freedom and redundant modes. Yang *et al.* [29] presented an efficient stability prediction method for large thin-walled workpieces based on the decomposition reduction strategy. Li *et al.* [30] applied a combination of a free-interface and a structural dynamic modification approach to further improve the computational efficiency. Karimi and Altintas [31] developed a fast shell element model to obtain the dynamics of thin-walled turbine blades. It is worth mentioning that Honeycutt and Schmitz [32] effectively estimated a variable dynamics of thin rib by using the receptance coupling method. All of the above discussed methods are used to calculate time-varying modal parameters of workpiece, based on which the dynamic SLDs are determined.

Besides stability prediction, chatter detection and suppression are also important contributors to efficient metal cutting processes [33,34]. Hence chatter is not only identified by a real-time online detection, but it is expected to be predicted at earlier stages of operation planning. Ji *et al.* [35] constructed a three-dimensional characteristic vector using an empirical mode decomposition and multi-indicator synthetic evaluation for an early identification of chatter. Cao *et al.* [36] proposed an adaptive chatter-signal-enhancement method for distinguishing an early weak chatter from strong disturbances. Rather than being limited to the time or frequency domains, identification methods should use all other available information to determine whether chatter has occurred [37-39]. Liu *et al.* [40] combined variational mode decomposition and energy entropy for the detection of chatter in machining processes. Li *et al.* [41] used the multiscale entropy method with a gradient tree boosting for online identification of chatter and intelligent diagnosis of chatter severity. Such detection methods can classify

signals whether chatter occurs or not and evaluate its severity. In addition of using SLDs to avoid chatter, there are some passive methods for chatter suppression such as vibration absorbers, tunable mass dampers, spindle speed variation, etc. [42-49]. Some scholars have also adapted other measures for specific machining processes, for example, Fei *et al.* [50] set a moving damper parallel to the main spindle and developed a damper-based SLD whilst Zhang *et al.* [51,52] designed a milling chatter suppression scheme using the viscous fluid. Wan *et al.*[53,54] adopted a method of attaching additional mass and prestressing, which also improved the stability boundary. Liu *et al.*[55] and Gibbons *et al.* [56] enhanced the stability boundary of SLD effectively by modifying the tool-holder. Munoa *et al.* [57] designed a tuneable clamping table to increase stability limits for milling of thin-walled workpieces. In essence, the mentioned above chatter suppression methods, can provide new means for improving stability of machining processes.

Although some progress has been made in predicting the SLD for thin-walled workpieces, to the best of our knowledge, a relatively little research has been done on continuous machining of general shape workpieces. The continuous radial immersion milling refers to consecutive milling passes of a workpiece in the radial direction using fixed machining parameters including axial depth of cut, spindle speed, feed per tooth and radial depth of cut, for entire roughing processes [58]. When a workpiece is continuously machined with low radial immersion, thickness of workpiece inevitably undergoes a change from thick to thin, which results in change of the workpiece dynamic properties. It is difficult to determine the dominant mode of the machining system where the flexibility of the tool and workpiece is not significantly different. Even during the machining of thin-walled workpiece with low stiffness, the mode of the workpiece does not always play a dominant role. Although the structural dynamic modification can be applied to obtain the time-varying modal parameters of the workpiece, the fine-meshing is required for the continuous immersion milling, which may lead to the problems of re-meshing and node determination. In addition, the workpiece is not necessarily in rigid contact with the vise, and the accurate mode shape extraction still needs to refer to a series of dynamic test results. Therefore, how to ensure stable machining parameters at each step of the continuous machining process and what measures should be used to improve the stability of the continuous machining process, are two very important aspects. The stability analysis for a complex shape workpiece under consecutive immersion milling passes still faces some challenges.

It is particularly important to design an effecting SLD to suppress chatter under continuous machining conditions, which is the main focus of this work, hence the paper is organized as follows. In Section 2, we propose a rapid method to obtain mode shapes and frequencies of a workpiece for a continuous radial immersion milling,

which is based on Timoshenko beam model and receptance coupling. In Section 3, the dynamic tests to identify the contact state between the workpiece and vise are presented, based on which the mode shapes of the workpiece under the prescribed clamping force were determined. In Section 4, the conservative SLD using the mode shape matrix and time-varying natural frequencies for different machining stages is constructed, and dynamic tests with different passive chatter suppression measures (additional cylinder masses and passive support) are discussed. In Section 5, modified conservative SLDs with two proposed chatter suppression measures are discussed. In Section 6, the conclusions and future research ideas are outlined.

2. Rapid determination of mode shapes and frequencies for continuous radial immersion milling

During the immersion milling, when material is continuously removed in the radial direction, the modal parameters of the workpiece show time-varying characteristics. For a FRF, mass-normalized mode shapes at certain natural frequencies determine amplitudes. When a mass-normalized mode shape becomes larger, a workpiece exhibits lower stiffness at this node. When undertaking stability analysis of the cutting process, a mass-normalized mode shape and natural frequency also affect stability limits corresponding to the state transition matrix. Therefore, mode shapes and natural frequencies of workpiece are essential to be carefully considered in stability analysis. This section introduces the receptance coupling method for a Timoshenko beam model, and shows how to extract mode shapes and natural frequencies for continuous radial immersion milling.

2.1. Receptance coupling for different machining stages

In continuous machining operations akin to the radial immersion milling where cuboids of material are being removed sequentially in stages, the workpiece can be simplified as coupled substructures shown schematically in Figure 1. In order to conveniently simulate material removal in continuous radial immersion milling, the workpiece is divided into four stages during the modeling process. Stage 1 is the assembly prior a radial material removal; Stage 2 is the assembly with a radial material removal of 8 mm; Stage 3 is the assembly with radial material removal of 12 mm and Stage 4 can be viewed as a substructure with the effective height reduced to 40 mm. For each specific machining stage, the workpiece is further divided into Substructure A, Substructure B and the part in contact with the vise. Therefore, these three parts correspond to three coordinates systems used to calculate the receptance couplings, as shown in Figure 1(a). Coordinates 1 and 2 are used to

describe the coupling relation between Substructures A and B, and Coordinate 3 is used to describe the coupling relation between the bottom of workpiece and the vise. At the coupling interface Coordinates 2 and 3 are further divided into Coordinates 2a, 2b and Coordinates 3a, 3b, respectively. As shown in Figure 1, a description of the translational and rotational movement of the substructures is facilitated by defining generalized receptance matrix as proposed in [59],

$$R_{\mathrm{uv}} = \begin{pmatrix} \dfrac{x_{\mathrm{u}}}{f_{\mathrm{v}}} = H_{\mathrm{uv}}, & \dfrac{x_{\mathrm{u}}}{\chi_{\mathrm{v}}} = L_{\mathrm{uv}} \\[2ex] \dfrac{\alpha_{\mathrm{u}}}{f_{\mathrm{v}}} = N_{\mathrm{uv}}, & \dfrac{\alpha_{\mathrm{u}}}{\chi_{\mathrm{v}}} = P_{\mathrm{uv}} \end{pmatrix}, \tag{1}$$

where x is the displacement, f is the force, α is the rotation angle, χ is the coupling; the subscripts v and u represent the excitation response locations respectively.
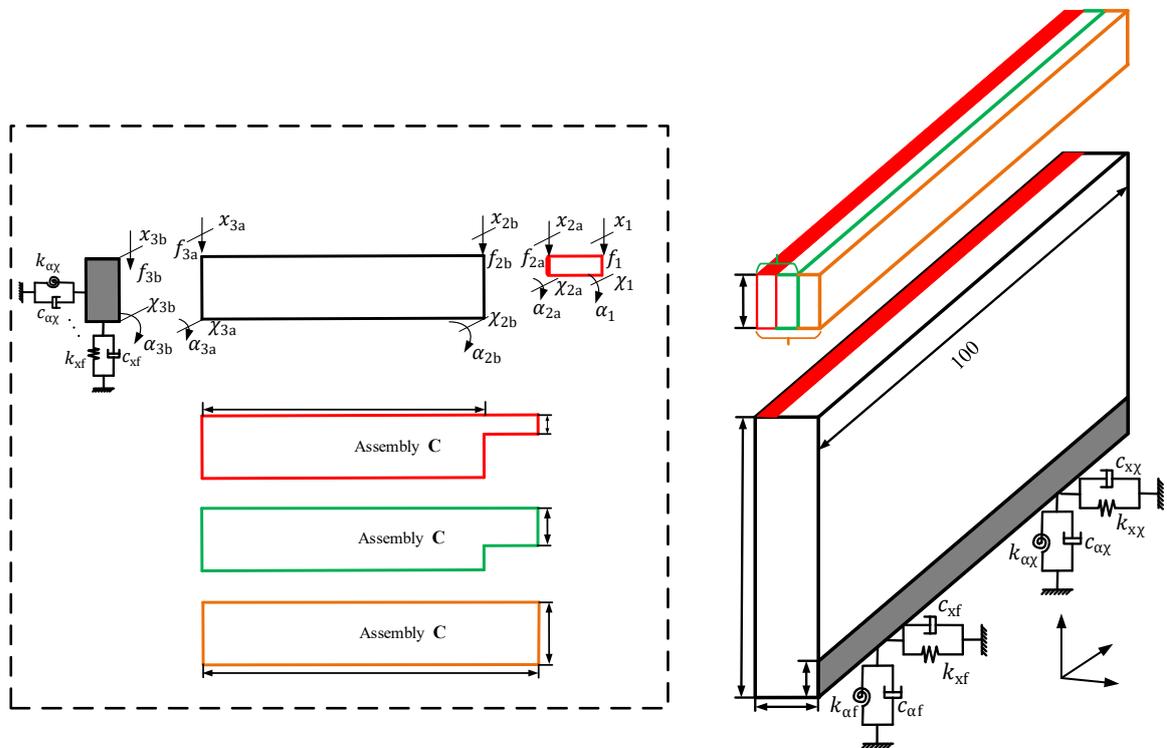

Figure 1. Physical modelling with the receptance coupling approach showing different machining stages; (a) dynamic model of the top free end; (b) flexible-damped coupling contact model for different machining stages. Stage 1 is the assembly prior a radial material removal; Stage 2 is the assembly with a radial material removal of 8 mm; Stage 3 is the assembly with radial material removal of 12 mm; Stage 4 can be viewed as a substructure with the effective height reduced to 40 mm. Substructures A and B are used for the receptance coupling.

In order to specify the elements of the generalized receptance matrix, the Timoshenko beam model is applied (see Appendix A for details). Based on the rigid coupling model of Substructures A and B depicted in Figure 1(a), the assembly receptance matrix between Coordinates 1 and 2, G_{11}, can be deduced as [32]:

$$G_{11} = \begin{pmatrix} H_{11} & L_{11} \\ N_{11} & P_{11} \end{pmatrix} = R_{11} - R_{12a}(R_{2a2a} + R_{2b2b})^{-1}R_{2a1}, \tag{2}$$

where G_{11} is the assembly receptance matrix at the top of the workpiece, and the generalized receptance matrices satisfy the definition in Eq.(1); R_{11} and R_{2a1} are generalized receptance matrices at Coordinates 1 and 2a when the harmonic force and bending couple are applied to Coordinate 1; R_{12a} and R_{2a2a} are generalized receptance matrices at Coordinates 1 and 2a when the harmonic force and bending couple are applied to Coordinate 2a; R_{2b2b} is generalized receptance matrix at Coordinate 2b when the harmonic force and bending couple are applied to Coordinate 2b. Consequently, as shown in Figures 1 and 2(a), the Substructures A and B together form the Assembly C, therefore, Eq. (1) can be rewritten as:

$$G_{11} = R_{11}^C = \begin{pmatrix} H_{11}^C & L_{11}^C \\ N_{11}^C & P_{11}^C \end{pmatrix} = R_{11}^A - R_{12}^A(R_{22}^A + R_{22}^B)^{-1}R_{21}^A, \tag{3}$$

where R_{uv}^A, R_{uv}^B, and R_{uv}^C are generalized receptance matrices of Substructure A, Substructure B and Assembly C respectively.

In Eq. (3), the generalized receptance matrices of Substructure A can be calculated from the Timoshenko beam model, while the receptance matrix of Substructure B, R_{22}^B, needs to be determined by coupling Substructure B and vise at Coordinate 3. It is important to note here that the contact state between the workpiece and fixture at Coordinate 3 is unknown when using the receptance coupling model. Apart from all possible effects caused by different clamping methods, a key factor is the clamping force. Therefore, it is necessary to construct a robust predictive model based on the measured FRF. When the flexible-damped coupling contact model is employed, a dynamic coupling matrix is introduced as:

$$K = \begin{bmatrix} k_{xf} + i\omega c_{xf} & k_{x\chi} + i\omega c_{x\chi} \\ k_{\alpha f} + i\omega c_{\alpha f} & k_{\alpha\chi} + i\omega c_{\alpha\chi} \end{bmatrix}, \tag{4}$$

where ω is angular frequency, $k_{xf} + i\omega c_{xf}$ is the stiffness and damping term which corresponds to the H_{uv} in Eq. (1), and this applies to the remaining three elements of the matrix.

With the dynamic coupling matrix considered, the assembly receptance matrix between Substructure B and vise, G_{22}, can be expressed as:

$$G_{22} = R_{22}^B = \begin{pmatrix} H_{22} & L_{22} \\ N_{22} & P_{22} \end{pmatrix} = R_{22} - R_{23a}(R_{3a3a} + R_{3b3b} + \text{inv}(K))^{-1}R_{3a2}, \tag{5}$$

where G_{22} is the assembly receptance matrix at the top of the Substructure B, and the generalized receptance matrices satisfy the definition in Eq.(1).

2.2. Mode shapes extraction and dynamic model

In the process stability assessment it is necessary to monitor incremental changes of the axial depth of cut, from which the dynamic cutting force considering the angular delay effect can be easily calculated by using the infinitesimal element approach. Therefore, the cutting edge is discretized into equal thickness elements by using sections parallel to the tool axis. These infinitesimal elements correspond to the axial depth of cut on the workpiece. As depicted in Figure 2, the milling tool is partitioned into s parts along the tool axis and the height of each element is Δb. When the regenerative effect is considered, the instantaneous uncut chip thickness of the jth tooth in Figure 2(c) can be written as:

$$h_j(t) = f_t \sin(\theta_j) + [\sin(\theta_j), \cos(\theta_j)][(q_{t,p}(t) - q_{t,p}(t - \tau)) - (q_{w,p}(t) - q_{w,p}(t - \tau))], \quad (6)$$

where f_t is the feed per tooth, θ_j is the instantaneous angular position for the jth tooth, τ is the time delay, $q_{t,p}$ is a projection of $\mathbf{q}_t(t) = \begin{bmatrix} x_t(t) \\ y_t(t) \end{bmatrix}$ and $q_{w,p}$ is a projection of $\mathbf{q}_w(t) = \begin{bmatrix} x_w(t) \\ y_w(t) \end{bmatrix}$. The instantaneous angular position having an angular delay effect can be defined as:

$$\theta_j = \theta_j(t, \mu * \Delta b) = \frac{2\pi\Omega}{60}t + (j-1)\frac{2\pi}{N} - (\mu - 1)\frac{2\tan\beta}{d}\Delta b, \qquad j = 1,2,\cdots,N; \mu = 1,2,\cdots,s; \quad (7)$$

where Ω is the spindle speed, N is the number of cutting teeth, d is the milling tool diameter and β is the helix angle. The infinitesimal dynamic cutting forces acting in X and Y directions can be calculated as a product of the effective relative dynamic deflection and the stiffness, which can be assembled as follows:

$$\begin{bmatrix} \Delta F_{t,\mu,x}(t) \\ \Delta F_{t,\mu,y}(t) \end{bmatrix} = \Delta b \sum_{j=1}^{N} g(\theta_j) \begin{bmatrix} -\cos(\theta_j) & -\sin(\theta_j) \\ \sin(\theta_j) & -\cos(\theta_j) \end{bmatrix} \begin{bmatrix} K_{tc} \\ K_{nc} \end{bmatrix} [\sin(\theta_j), \cos(\theta_j)]$$

$$\text{x } [(q_{t,p}(t) - q_{t,p}(t - \tau)) - (q_{w,p}(t) - q_{w,p}(t - \tau))], \quad (8)$$

where $g(\theta_j) = \begin{cases} 1 & \theta_{en} < \theta_j < \theta_{ex}, \\ 0 & \theta_j < \theta_{en} \ or \ \theta_j > \theta_{ex}, \end{cases}$ $(j = 1,2,\cdots,N)$, $g(\theta_j)$ is the Heaviside's step function, θ_{en} is the entry angle and θ_{ex} is the exit angle, K_{tc} and K_{nc} are the cutting force coefficients in tangential and normal directions. Now, the force acting on the milling tool can be expressed as:

$$\mathbf{F}_t(t) = \sum_{\mu=1}^{s} \begin{bmatrix} \Delta F_{t,\mu,x}(t) \\ \Delta F_{t,\mu,y}(t) \end{bmatrix} = -\mathbf{F}_w(t), \quad (9)$$

where $\mathbf{F_w}(t)$ is the force acting on the workpiece. In general, the dynamics of this machining process is strongly and inherently nonlinear (see e.g. [60, 61, 62]), however for the fixed process parameters and assuming that the tool is in contact with the workpiece, it can be described the following linearized matrix equation of motion:

$$\mathbf{M\ddot{Q}}(t) + \mathbf{C\dot{Q}}(t) + \mathbf{KQ}(t) = \mathbf{F}(t), \tag{10}$$

where the mass matrix $\mathbf{M} = \begin{bmatrix} \mathbf{M_t} & \\ & \mathbf{M_w} \end{bmatrix}$, the damping matrix $\mathbf{C} = \begin{bmatrix} \mathbf{C_t} & \\ & \mathbf{C_w} \end{bmatrix}$, the stiffness matrix $\mathbf{K} = \begin{bmatrix} \mathbf{K_t} & \\ & \mathbf{K_w} \end{bmatrix}$, $\mathbf{Q(t)} = \begin{bmatrix} \mathbf{q_t}(t) \\ \mathbf{q_w}(t) \end{bmatrix}$ and $\mathbf{F(t)} = \begin{bmatrix} \mathbf{F_t}(t) \\ \mathbf{F_w}(t) \end{bmatrix}$
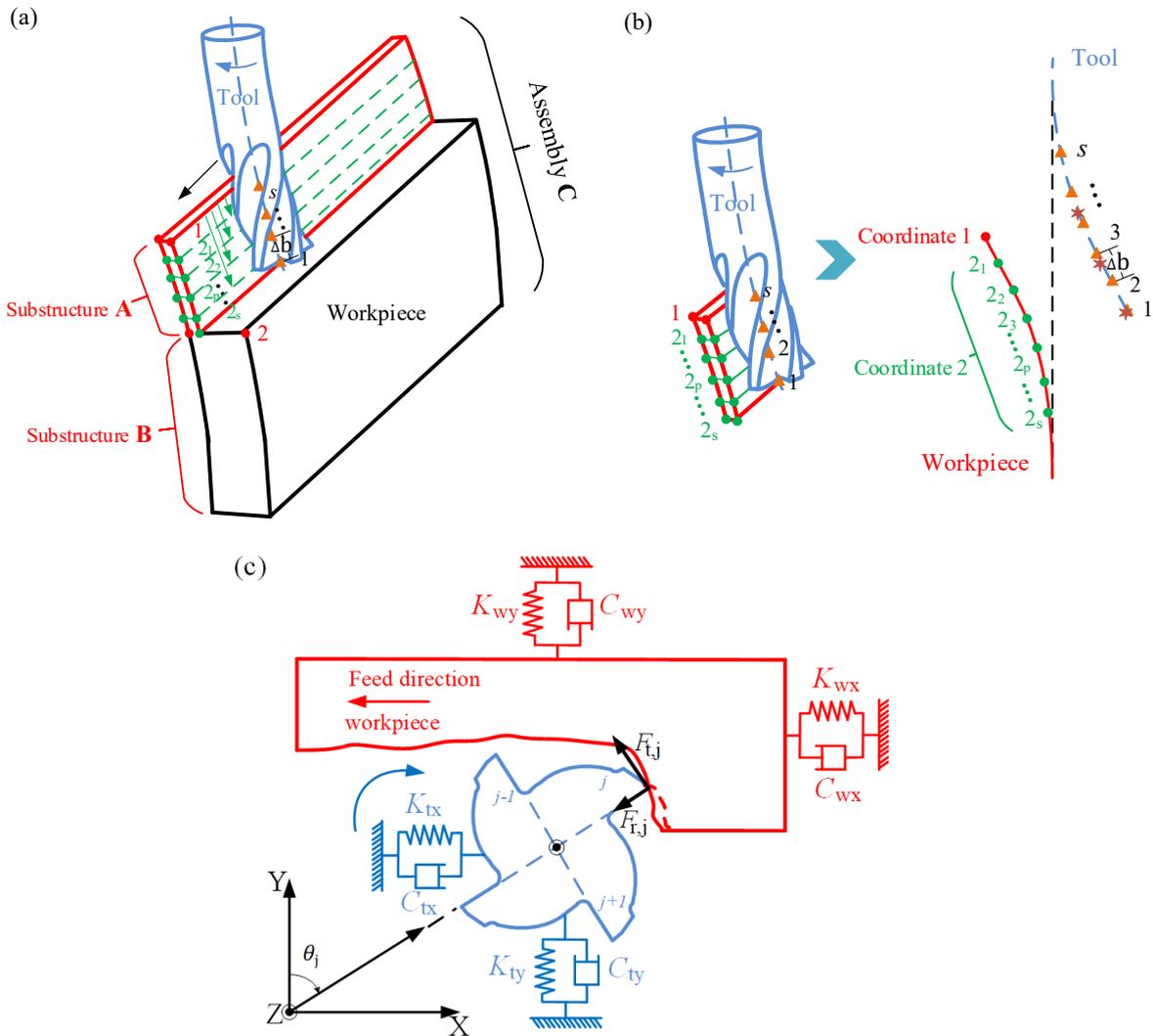
Figure 2. Mode shapes determination by the receptance coupling method; (a) receptance model for different relative positions of the tool and the workpiece ($2_p, p = 1,2,\cdots s$, 2_p represents a possible position of assembly receptance); (b) discretization scheme of the milling tool and corresponding interpolation scheme of the workpiece; (c) two degrees-of-freedom model of the up-milling process. Substructure B is viewed as the base and the mode shapes are identified from Assembly C. The blue line represents the milling tool and the red line represents the workpiece. In Figure 2(a, b), the triangles represent discretization points on the milling tool;

the circles represent assembly receptances of possible positions on the workpiece; the six-pointed stars represent response points measured during dynamic tests on the tool tip point.

Now Eq. (10) which describes the dynamics of the modelled process, can be transformed to the modal form and consequently its modal matrices, and then evaluated via the experimental modal testing. Specifically, the FRFs of the workpiece having time-varying modal parameters and the tool need to be determined. First, the Fourier transformation of the workpiece equation of motion is performed and this results in the following expression:

$$(i\omega)^2 \mathbf{M_w q_w}(\omega) + (i\omega)\mathbf{C_w q_w}(\omega) + \mathbf{K_w q_w}(\omega) = \mathbf{F}_w(\omega), \tag{11}$$

where $\mathbf{M_w}$ is the modal mass of the workpiece, $\mathbf{q_w}(\omega)$ is the workpiece dynamic displacement in frequency domain, $\mathbf{C_w}$ is the damping of the workpiece, $\mathbf{K_w}$ is the stiffness of the workpiece and $\mathbf{F_w}(\omega)$ is the force acting on the workpiece in frequency domain. In order to decouple the modes in the workpiece subsystem, the modal transformation $\mathbf{q_w}(t) = \boldsymbol{\phi_w}\boldsymbol{\Gamma_w}(t)$ is applied and after the mass normalization, the FRF of the workpiece subsystem can be written as:

$$\begin{cases} -\omega^2\boldsymbol{\phi_w^T M_w \phi_w \Gamma_w}(\omega) + (i\omega)\boldsymbol{\phi_w^T C_w \phi_w \Gamma_w}(\omega) + \boldsymbol{\phi_w^T K_w \phi_w \Gamma_w}(\omega) = \boldsymbol{\phi_w^T F_w}(\omega), \\ \qquad \mathbf{H}(\omega) = \dfrac{\mathbf{q_w}(\omega)}{\mathbf{F_w}(\omega)} = \dfrac{\boldsymbol{\phi_w}\boldsymbol{\Gamma_w}(\omega)}{\mathbf{F_w}(\omega)} = \displaystyle\sum_{r=1}^{n_w} \dfrac{\{\phi_w\}_r\{\phi_w^T\}_r}{\omega_r^2 - \omega^2 + i2\zeta_r\omega_r\omega}, \end{cases} \tag{12}$$

where $\boldsymbol{\phi_w}$ is the mass-normalized mode shape of workpiece, $\omega_r = \sqrt{\dfrac{K_w}{M_w}}$ is the natural frequency of the rth mode, and $\zeta_r = \dfrac{C_w}{2\sqrt{M_w K_w}}$ is the damping ratio.

During the material removal process, the FRF of the tool does not change much so it can be regarded as a constant. When the FRF of the milling tool is analyzed, a similar result to Eq. (12) can be obtained. The difference is that the mass-normalized mode shape and the natural frequency in Eq. (12) are time-varying during the material removal process, while the two parameters are constant for the milling tool. Therefore, the modal parameters of the milling tool are mainly obtained from dynamic tests. The milling tool is excited at the tool tip point and the responses are measured at the three points of the milling tool (see Figure 2(b)), and then the mode shape function along the tool axis is fitted. According to the discretization scheme of the milling tool, the mode shape matrices of the milling tool and workpiece are obtained by interpolation and receptance coupling. As a result, the mass-normalized mode shape matrices of the milling tool and workpiece in *X* and *Y* direction can be defined as:

$$\Phi_t = \Phi_{t,s} = \begin{pmatrix} \phi_{x1,1,t} & \phi_{x1,2,t} & \cdots & \phi_{x1,n_t,t} \\ \phi_{y1,1,t} & \phi_{y1,2,t} & \cdots & \phi_{y1,n_t,t} \\ \vdots & \vdots & \ddots & \vdots \\ \phi_{x\mu,1,t} & \phi_{x\mu,2,t} & \cdots & \phi_{x\mu,n_t,t} \\ \phi_{y\mu,1,t} & \phi_{y\mu,2,t} & \cdots & \phi_{y\mu,n_t,t} \\ \vdots & \vdots & \ddots & \vdots \\ \phi_{xs,1,t} & \phi_{xs,2,t} & \cdots & \phi_{xs,n_t,t} \\ \phi_{ys,1,t} & \phi_{ys,2,t} & \cdots & \phi_{ys,n_t,t} \end{pmatrix}_{2s \times n_t}, \qquad (13)$$

$$\Phi_w = \Phi_{w,s} = \begin{pmatrix} \phi_{x1,1,w} & \phi_{x1,2,w} & \cdots & \phi_{x1,n_w,w} \\ \phi_{y1,1,w} & \phi_{y1,2,w} & \cdots & \phi_{y1,n_w,w} \\ \vdots & \vdots & \ddots & \vdots \\ \phi_{x\mu,1,w} & \phi_{x\mu,2,w} & \cdots & \phi_{x\mu,n_w,w} \\ \phi_{y\mu,1,w} & \phi_{y\mu,2,w} & \cdots & \phi_{y\mu,n_w,w} \\ \vdots & \vdots & \ddots & \vdots \\ \phi_{xs,1,w} & \phi_{xs,2,w} & \cdots & \phi_{xs,n_w,w} \\ \phi_{ys,1,w} & \phi_{ys,2,w} & \cdots & \phi_{ys,n_w,w} \end{pmatrix}_{2s \times n_w},$$

where Φ_t is the mass-normalized mode shape matrix of the milling tool, n_t is the number of excited mode of milling tool, Φ_w is the mass-normalized mode shape matrix of the workpiece, n_w is the number of excited mode of workpiece and *s* is the discretization number of the milling tool.

At different machining stages, the mass-normalized mode shapes of the workpiece exhibit time-varying characteristics. For the workpiece, it is necessary to obtain the mode shapes of Assembly C at different machining stages and positions along the cutting edge (See 2_p in Figure 2(a, b)). Like Eq. (2), the assembly receptance at Coordinate 2 in Figure 1(a) can also be directly developed as:

$$R_{22}^C = R_{22}^A - R_{22}^A (R_{22}^A + R_{22}^B)^{-1} R_{22}^A. \qquad (14)$$

From Figure 2 and Eq. (14), it can be seen that the R_{22}^C at different positions needs to continuously obtain the latest R_{22}^B. That is, in the case of a specific axial depth of cut, multiple terms of R_{22}^B are required to obtain the mass-normalized mode shapes at different positions along the cutting edge (see 2_p in Figure 2(a, b)). Therefore, it is better to implicitly omit the term of R_{22}^B in the determination of the mass-normalized mode shapes of the workpiece, and Eq. (14) can be changed as:

$$R_{22}^B = -R_{22}^A + R_{22}^A (R_{22}^A - R_{22}^C)^{-1} R_{22}^A. \qquad (15)$$

After substituting Eq. (15) into Eq. (3), the receptance at the free end of the workpiece and point on the same component can be expressed mutually [63]. Therefore, the assembly receptance at Coordinate 2 can be rewritten as:

$$R_{22}^C = \begin{pmatrix} H_{22}^c & L_{22}^c \\ N_{22}^c & P_{22}^c \end{pmatrix} = R_{22}^A - R_{22}^A R_{12}^{A-1} \left(R_{11}^A - R_{11}^C \right) R_{21}^{A-1} R_{22}^A. \tag{16}$$

According to Eq. (16), once R_{11}^C is determined, the assembly receptance of R_{22}^C at different positions no longer depends on R_{22}^B, but depends on the generalized receptance of Substructure A. It can be seen from Eq. (3) that the term of R_{22}^B only needs to be determined once according to the contact state when determining R_{11}^C, instead of repeatedly obtaining the term of R_{22}^B. Based on the assembly receptance at the Coordinate 1 and the generalized receptance of the Substructure A, as shown in Figure 2, the assembly receptance at the Coordinate 2 can be determined from Eq. (16). It is worth to note here that the position of Coordinate 2 varies with the axial depth of cut. By combining Eqs. (12) and (16), the mass-normalized mode shapes at contact zone between milling tool and workpiece can be obtained and expressed as follows:

$$H_{22}^c(\omega) = \sum_{r=1}^{n_w} \frac{\{\phi_2^c\}_r \{\phi_2^c\}_r}{\omega_r^2 - \omega^2 + i2\zeta_r \omega_r \omega} = \frac{\{\phi_2^c\}_1 \{\phi_2^c\}_1}{\omega_1^2 - \omega^2 + i2\zeta_1 \omega_1 \omega} + \cdots + \frac{\{\phi_2^c\}_{n_w} \{\phi_2^c\}_{n_w}}{\omega_{n_w}^2 - \omega^2 + i2\zeta_{n_w} \omega_{n_w} \omega}, \tag{17}$$

where $\{\phi_2^c\}_1 = \phi_{y\mu,1,w}$, ϕ_2^c is the mass-normalized mode shape of workpiece at the Coordinate 2 and n_w is the number of excited mode of workpiece.

For continuous machining processes, the modal frequencies and mode shapes of the workpiece show time-varying characteristics. These time-varying parameters make the SLD exhibit dynamic changes, which causes significant challenges in robust stability prediction. To overcome these difficulties, it is possible to construct a conservative SLD where the goal is not necessarily the maximum material removal rate, but rather to obtain stable processing parameters. As can be seen in Eq. (13), the number of rows of the workpiece's mode shape matrix varies with s, which increases with the increase of the axial depth of cut. For the same machining stage, the number of rows of the mode shape matrix is not the same for different axial depths of cut. Therefore, the maximum value of each row of the different mode shape matrices in the same machining stage is taken to develop the updated mode shape matrix and the updated mode shape matrix satisfy the following relation:

$$\begin{cases} \mathbf{\Phi}_{wu} = \max\ \{\mathbf{\Phi}_{w,1}, & \mathbf{\Phi}_{w,2}, & \cdots & \mathbf{\Phi}_{w,s}\}, \\ \mathbf{\Phi}_w = \mathbf{\Phi}_{wu}, \end{cases} \tag{18}$$

where $\mathbf{\Phi}_{wu}$ is the updated mode shape matrix of the workpiece, $\mathbf{\Phi}_{w,s}$ is the mode shape of the sth row and $\mathbf{\Phi}_w$ is mode shape matrix of the workpiece. The mass-normalized mode shapes of the Assembly C at different depths of cut can be extracted by combining Eqs. (16-18), which is different from the modal parameters obtained in Ref. [32], where the dynamics is determined at the top of the Assembly C according to Eq. (2).

In the process of obtaining the above mass-normalized mode shape matrices, the coordinate transformation is used to normalize the mass matrix. This coordinate transformation not only decouples the multiple modes, but also makes the dynamic equation more concise. Therefore, solving Eq. (10) in the modal coordinates system further simplifies the calculation process and the system dynamics in the modal space becomes:

$$\ddot{\mathbf{\Gamma}}(t) + 2\boldsymbol{\xi}\boldsymbol{\omega}\dot{\mathbf{\Gamma}}(t) + \boldsymbol{\omega}^2\mathbf{\Gamma}(t) = \mathbf{\Phi}\mathbf{F}(t), \tag{19}$$

where $\boldsymbol{\xi} = \begin{bmatrix} \xi_t & \\ & \xi_w \end{bmatrix}$, $\boldsymbol{\omega} = \begin{bmatrix} \omega_t & \\ & \omega_w \end{bmatrix}$, $\mathbf{\Gamma(t)} = \begin{bmatrix} \mathbf{\Gamma}_t(t) \\ \mathbf{\Gamma}_w(t) \end{bmatrix}$, $\mathbf{F(t)} = \begin{bmatrix} \mathbf{F}_t(t) \\ \mathbf{F}_w(t) \end{bmatrix}$, and $\mathbf{\Phi} = \begin{bmatrix} \mathbf{\Phi}_t^T & \\ & -\mathbf{\Phi}_w^T \end{bmatrix}$.

3. Dynamic tests and identification of contact state parameters

The contact between the workpiece and the fixture characterizes the FRF of the workpiece in the clamped conditions. The dynamic tests of the workpiece can not only replicate the real contact state, but also analyze the effect of different clamping forces on the natural frequency of the workpiece. The following section introduces the experimental scheme for dynamic tests and the analysis of how different clamping forces can affect the natural frequency of the workpiece. Combining the experimental results with the theoretical predictions from Section 2, the contact state between the workpiece and vise was determined. Finally, based on the dynamic coupling matrix, the time-varying modal parameters of the workpiece under given clamping force were computed.

3.1. Dynamic tests for different clamping forces

Dynamic tests of the workpiece under a prescribed clamping force are the key to obtain accurate FRFs. As shown in Figure 3, the static force sensor is fixed to the movable end of the vise jaw with one washer, and the vise screw is placed on the hemisphere of the other washer. After the clamping force was applied to the vise, there was a small gap between the washers and the static force sensor. The force decayed slowly and showed small fluctuations, specifically, for the prescribed clamping force of 3000 N, the actual clamping force value had fluctuated between 2950 and 3050 N.
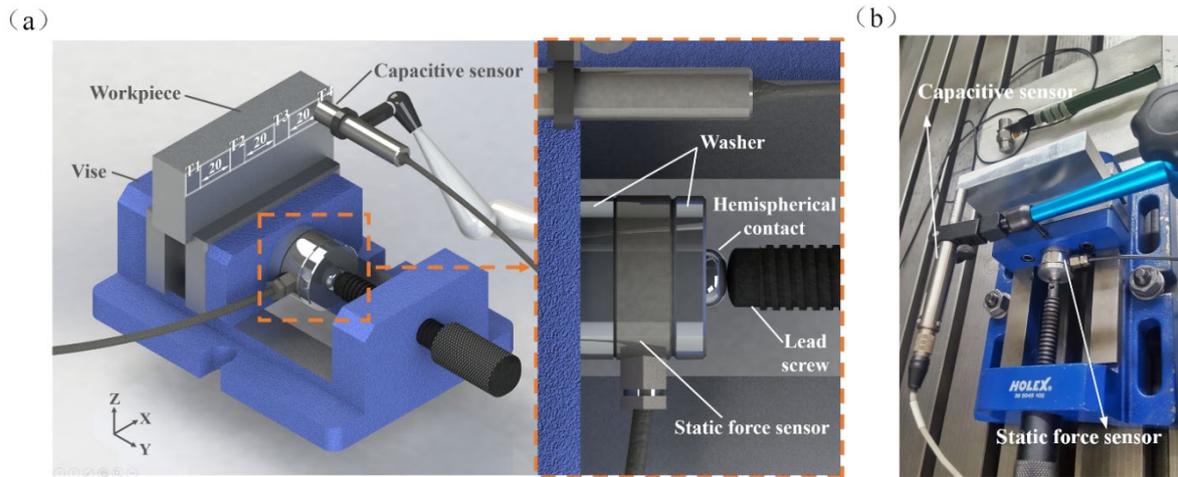
Figure 3. Dynamic tests with the prescribed clamping forces; (a) schematic representation for dynamic tests; (b) non-contact measurement setup for the FRF of workpiece. T1, T2, T3 and T4 are distribution of the four test regions in X direction, and the length of each test region is 10 mm. The capacitive sensor was employed to obtain the FRF at the four test regions and the lead screw was used to adjust the static force applying to vise.

The dynamics under four different machining stages were tested according to the division of the workpiece stages shown in Figure 1. For the hammer tests, the capacitive sensor was used to collect the response from the workpiece, and the excitation points of the force hammer and the measurement points were theoretically at the same location. As shown in Figure 3(a), four regions (T1, T2, T3 and T4) were selected along the tool path (i.e., X-direction) to obtain the FRFs. Since the diameter of the force hammer is 10 mm, the length of each test region is selected to be 10 mm. From Figure 4 (a)-(d), the first mode of the workpiece increased from 1425 Hz, through 1540 Hz and 1595 Hz to 1624 Hz when the workpiece shape changed between Stages 1 and 4. However, the amplitudes of the four different machining stages changed very little and remained in a relatively stable range. For each machining stage, the FRFs of T1 and T4 were close to each other, and the FRFs of T2 and T3 were also close to each other. This was mainly because the first mode corresponded to bending and the mode shapes at the top of the workpiece were nearly the same. For the second mode, the amplitudes at T2 and T3 were almost zero because the test regions T2 and T3 were closer to the nodes of the second mode than that of T1 and T4. In addition, the natural frequency of the second mode of the workpiece fluctuated between 5000 and 5500 Hz, and its amplitude was very low. Compared with the first mode, the natural frequency of the second mode was higher and far from the first mode, which was less likely to be excited during machining process. Therefore, only the first mode of the workpiece at different machining stages was considered.
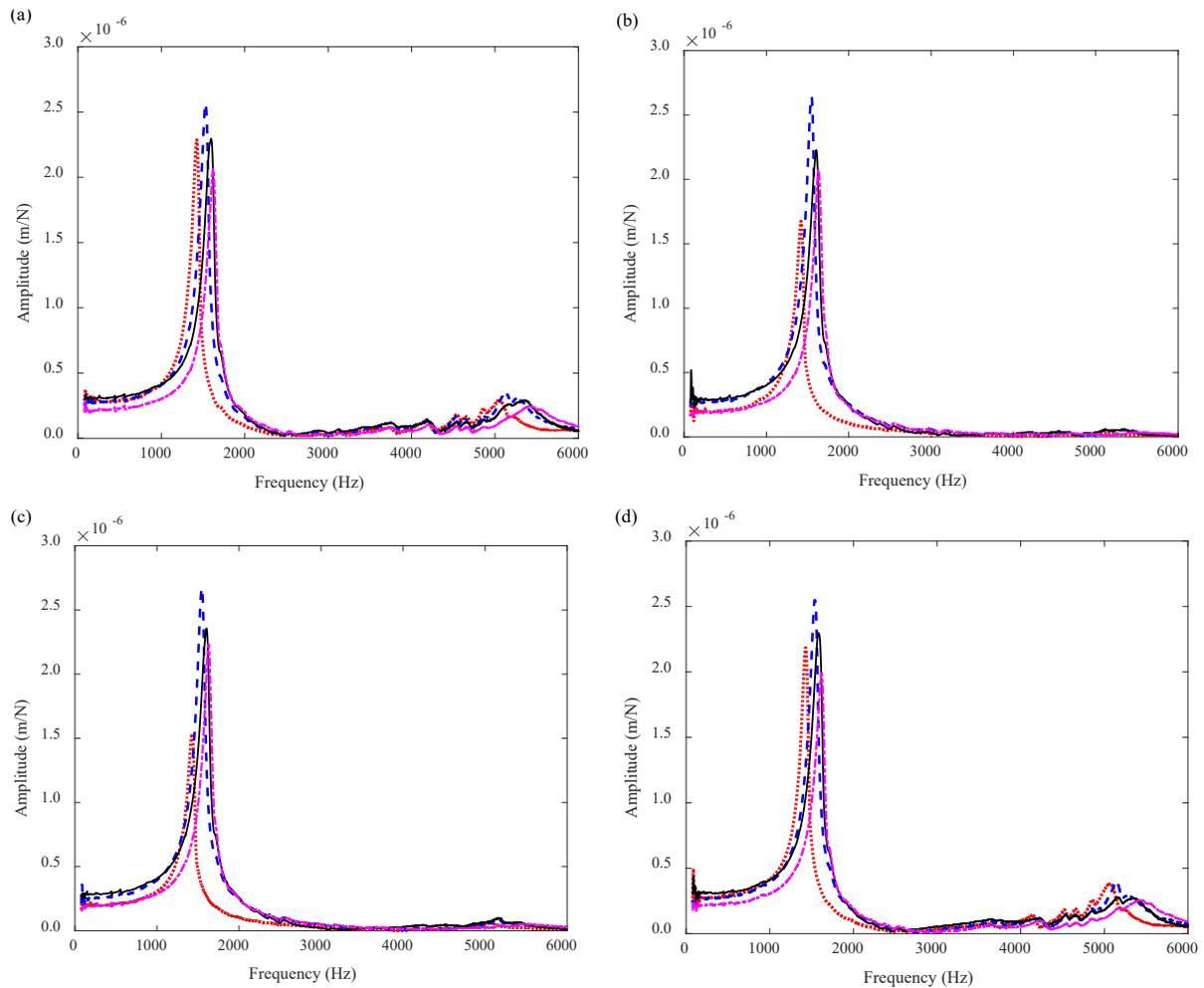
Figure 4. Dynamic tests of workpiece with the clamping force of 3000 N; (a) FRF of workpiece at T1; (b) FRF of workpiece at T2; (c) FRF of workpiece at T3; (d) FRF of workpiece at T4. Stage 1 is shown in red; Stage 2 is shown in blue; Stage 3 is shown in black; Stage 4 is shown in pink. Stage 1 is the assembly prior a radial material removal; Stage 2 is the assembly with a radial material removal of 8 mm; Stage 3 is the assembly with radial material removal of 12 mm; Stage 4 can be viewed as a substructure with the effective height reduced to 40 mm.

Following the same test procedure, the clamping force was adjusted to 1000 N, 2000 N and 4000 N, which resulted in the natural frequencies of the first mode at Stage 1 of 1260 Hz, 1390 Hz and 1550 Hz, respectively. The natural frequency of the first mode increased gradually with the increase of the clamping force, which indicated that the change of the clamping force could affect the contact state between the bottom end of the workpiece and the vise, and then affect the FRF of the workpiece. Therefore, the dynamic tests for the workpiece should be performed under the specific clamping force to ensure that the measured value can be accurately applied to the relevant machining stage.

3.2. Determination of contact state between workpiece and vise

Due to differences in clamping height and clamping force, the contact state between the workpiece and vise would change, which can be expressed by the parameters in dynamic coupling matrix. The contact state between the workpiece and vise is determined by comparing the theoretical value with the actual measured value. It is necessary to assume that the workpiece is in rigid contact with the vise in advance when calculating the theoretical value. If the theoretical value is close to the measured value, the workpiece is considered to be in rigid contact with the vise. Otherwise, the workpiece is regarded to be in a flexible contact with the vise. In this case, the stiffness and damping coefficients need to be identified according to the flexible-damped coupling model. Starting with Stage 1 in which the workpiece is uncut with its cuboid geometry is 100×45×15 mm, made of aluminum alloy 2007 with Young's modulus 71 GPa and Poisson's ratio 0.33, the computed natural frequency of the first mode using Ansys was 5874 Hz.

The FRF for the rigid connection between the workpiece and vise can be evaluated from Eq. (2). Under such connections, the natural frequency of the first mode with Timoshenko beam model at Stage 1 was 6030 Hz (see Figure A-1 in Appendix A), while the Ansys simulation result was 5874 Hz. The error between the two results was 2.6%, which shows that the rigid connection model can accurately predict the FRF. However, the measured natural frequency of the first mode at Stage 1 with clamping force of 3000 N was 1425 Hz, which differs from the natural frequency of the workpiece. It means that the actual contact state between the workpiece and vise is flexible and a modification is needed to cater for a more flexible and damped connection. It is therefore necessary to determine the parameters of the so-called dynamic coupling matrix, which can be employed to predict the FRFs for other machining stages. The dynamic equation is solved by using the maximum mass-normalized mode shapes at different discretization points, hence the test results at T1 are used to identify the parameters of the dynamic coupling matrix. It can be noted from Figure 4 that at the same machining stage, the frequencies of the first mode measured for all test regions differ slightly whilst their corresponding amplitudes significantly more.

3.3. Identification for the dynamic coupling matrix and time-varying modal parameters

Owing to complexity of damping mechanisms in mechanical connections, dynamic tests are used to determine damping. The equivalent viscous damping ratio of the workpiece identified from the dynamic tests is around 2.5%, which is similar to values reported in [64, 65], mainly used for convergence and stiffness analysis. Hence, the equivalent viscous damping ratio assumed in our studies is 0.025 and this value is used to compute the dynamic

stiffness via Eq. (4). The stiffness mainly controls the contact state, and its value can be chosen by minimizing the norm presented in Eq. (20):

$$\min_{K}\left\|\left|FRF_{\mathrm{sim}}\right| - \left|FRF_{\mathrm{exp}}\right|\right\|_{2}^{2},\tag{20}$$

where FRF_{sim} is the simulated FRF in Eq. (16), FRF_{exp} is the experimental FRF, and K is the dynamic coupling matrix. There are many methods for solving Eq. (20), but here we used the global gradient optimization algorithm with the nonlinear least-squares solver of Matlab. The identified parameters of the dynamic coupling matrix are shown in Tab. 1. With the damping ratio value of around 0.025, its influence on the identified parameters can be neglected. The predicted FRF of the workpiece at different machining stages with the flexible-damped coupling model is shown in Figure 5 and when compared with Figure 4, the flexible-damped coupling model is much closer to the test results, hence it is used for frequency and mode shapes extraction.

Tab. 1 Identified parameters of the dynamic coupling matrix

Stiffness term	k_{xf} (N/m)	$k_{\mathrm{x\chi}}$ (N-m/m)	$k_{\mathrm{\alpha f}}$ (N/rad)	$k_{\mathrm{\alpha\chi}}$ (N-m/rad)
Value	267	7.80×10^4	72.0	4.14×10^3
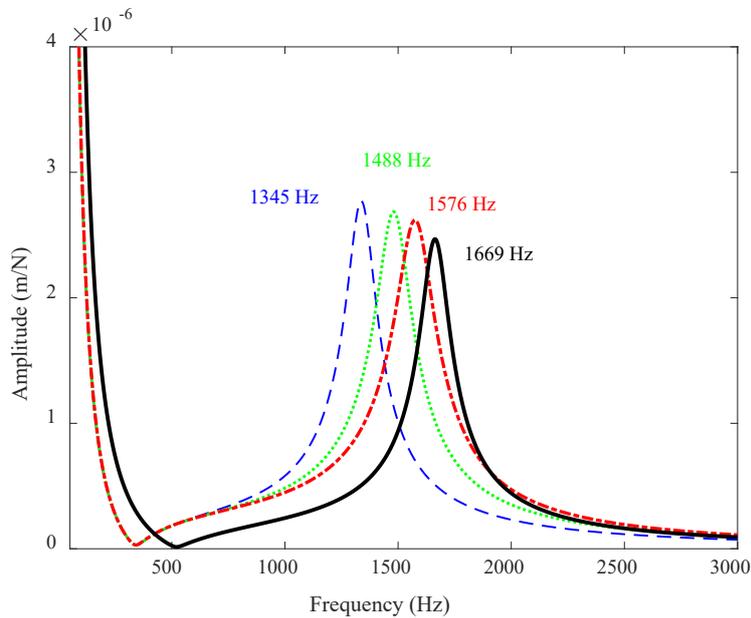
Figure 5. FRFs of the workpiece after modifications. The blue line shows the FRF of the workpiece at Stage 1; the green line shows the FRF of the workpiece at Stage 2; the red line shows the FRF of the workpiece at Stage 3; the black line shows the FRF of the workpiece at Stage 4.

According to Eqs. (16) and (17), the receptance at the top of the assembly can be converted into the receptance at any position on the assembly, and the related terms of Substructure B are implicit. The mode shapes of the assembly only need the receptance of Substructure A and Assembly C (see Figure 2(a)). According to the FRF of the different axial depths of cut, the mode shapes and time-varying frequency for different radial milling lengths are then presented in Figure 6. When comparing the dynamic test results at different machining stages shown in Figure 4, it can be found that the frequency variation range in Figure 6(c) is in good agreement with the dynamic test results both showing an increasing trend. Although the maximum mass-normalized mode shapes are adopted at the discretization nodes, the value of mass-normalization mode shape presented in Figure 6(a) is small, which leads to less significant changes in the amplitude of FRF. This is also consistent with the dynamic test results at T1 in Figure 4(a). Similar to the above, the predicted FRFs in Figure 5 also match well with Figure 6 when the flexible-damped coupling model is applied. Figure 6 indicates that with the radial milling length increase, the mode shapes and natural frequencies at different axial depths show a slow increasing trend. When the radial milling length is greater than 6 mm, the change of frequency is more evident, which further indicates that the modal parameters of the workpiece change very drastically as the radial material is continuously removed.
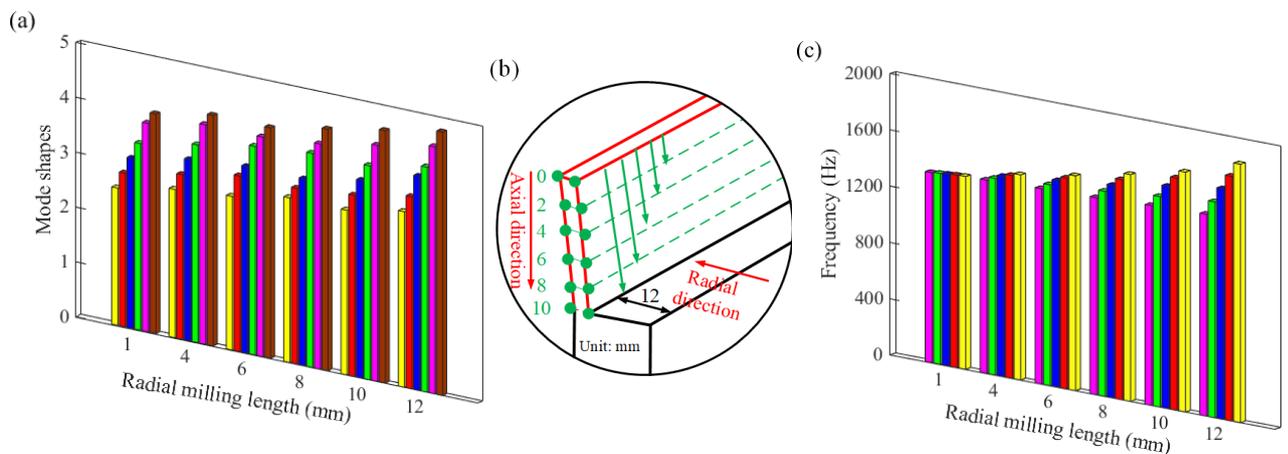
Figure 6. Determination of mass-normalized mode shapes and frequency; (a) mode shape variation in Y direction with material removal in radial and axial directions; (b) schematic illustration of the length in the axial and radial directions; (c) Frequency variation with material removal in axial and radial directions. The yellow column is the ADOC of 10 mm; the red column is the ADOC of 8 mm; the blue column is the ADOC of 6 mm; the green column is the ADOC of 4 mm; the pink column is the ADOC of 2 mm; the grey column is the ADOC of 0 (ADOC is short for Axial Depth in of Cut).

4. Conservative SLD and passive chatter suppression measures

The SLD is an important tool to predict the stability during continuous radial immersion milling process. To further enhance the boundary of the SLD and improve the material removal rate, passive chatter suppression measures can be employed. This section shows how to create a conservative 3D SLD using the modal parameters of the milling tool and the time-varying modal parameters of the workpiece. In order to suppress chatter, two modifications of the workpiece with additional cylinder masses and a passive support are explored. As the FRF can reflect the dynamic characteristics of the workpiece, the FRFs of the two modifications are analyzed.

4.1. Development of 3D SLD for continuous radial immersion milling process

In order to construct a conservative SLD for general workpiece with continuous machining, in addition to the time-varying modal parameters of workpiece, the modal parameters of the milling tool and the cutting force coefficients also need to be measured and identified. The modal parameters of the tool are obtained by using capacitive sensor and force hammer, and the measurement procedure was described in [66]. The damping ratio of the workpiece identified from the data to construct Figure 5 is 0.025, and the mass-normalized modal parameters are shown in Table 2.

Table 2. Measured mass-normalized two first mode shapes for the milling tool in feed and normal directions

Directions	Number of modes	Natural frequencies (Hz)	Damping ratio (%)	Normalized mode shape size $(1/\sqrt{\text{kg}})$
Feed direction	1	3122	2.5	[2.56 1.70 0.98]
	2	3814	2.8	[1.24 1.15 0.95]
Normal direction	1	3165	2.1	[2.83 1.82 1.13]
	2	3873	2.6	[1.35 1.07 0.54]

In the milling experiment, a four-fluted carbide end mill with diameter of 10 mm is applied and the helix angle of the milling tool is 30°. The linear cutting force model is employed to calibrate the cutting force coefficients as proposed in [67], and the results are as follows [65]: $K_{tc} = 1.03 \times 10^9$ Pa, $K_{nc} = 5.15 \times 10^8$ Pa.
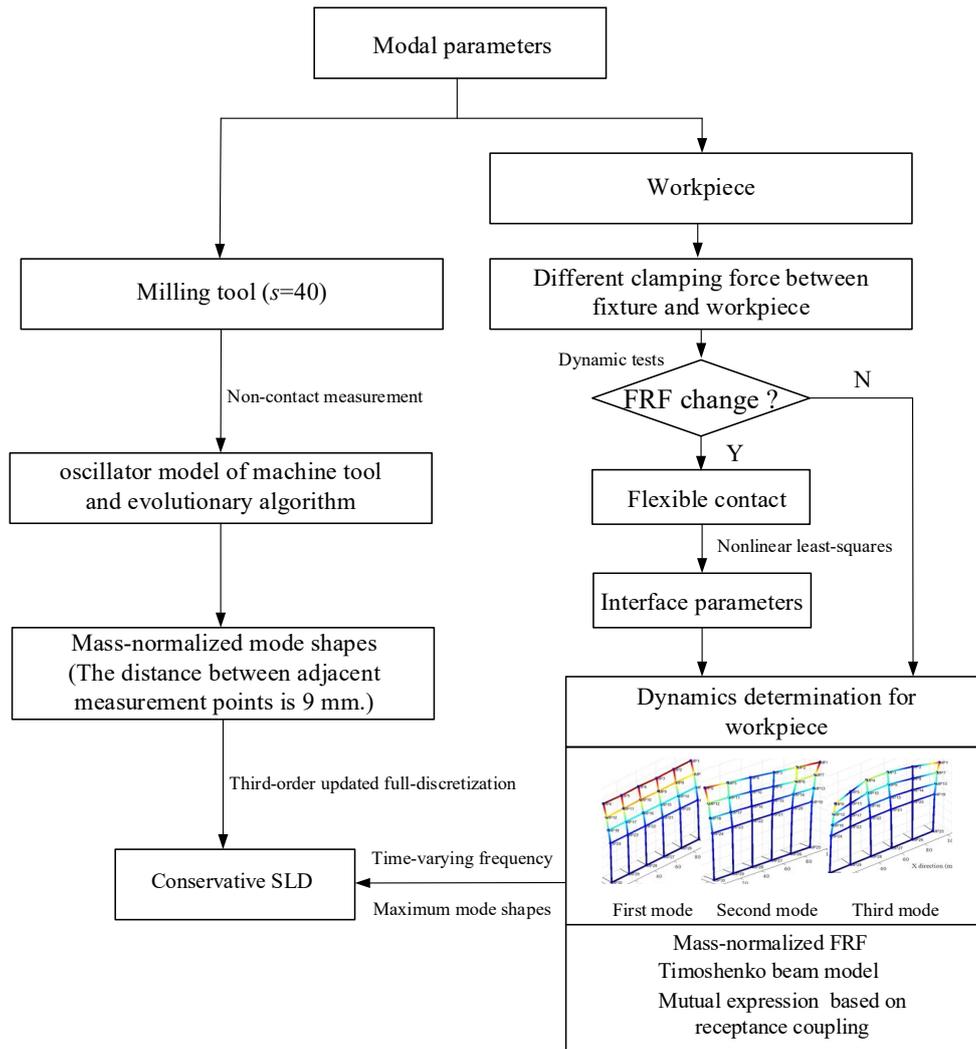
Figure 7. Flowchart of the conservative 3D-SLD with considering both dynamics of the milling tool and workpiece. The modal parameters of milling tool is measured with capacitive sensor, and the time-varying dynamics of workpiece is determined by receptance coupling and dynamic tests. The above modal parameters are used to develop the conservative SLD with a third-order updated full-discretization method.

Compared with Y direction, the mass-normalized mode shapes in X direction varies very slightly, which can be obtained from the element stiffness and mass matrices of the workpiece, and its variation ranges from 2×10^{-3} to 3×10^{-3}. The low radial immersion ratio is 10% (1 mm) with the feed per tooth of 0.1 mm/tooth. Following the procedures outlined in Figure 7, the third-order updated full-discretization method is employed to solve the dynamic equation [68], and the conservative SLD under the clamping force of 3000 N is then established, as shown in Figure 8.
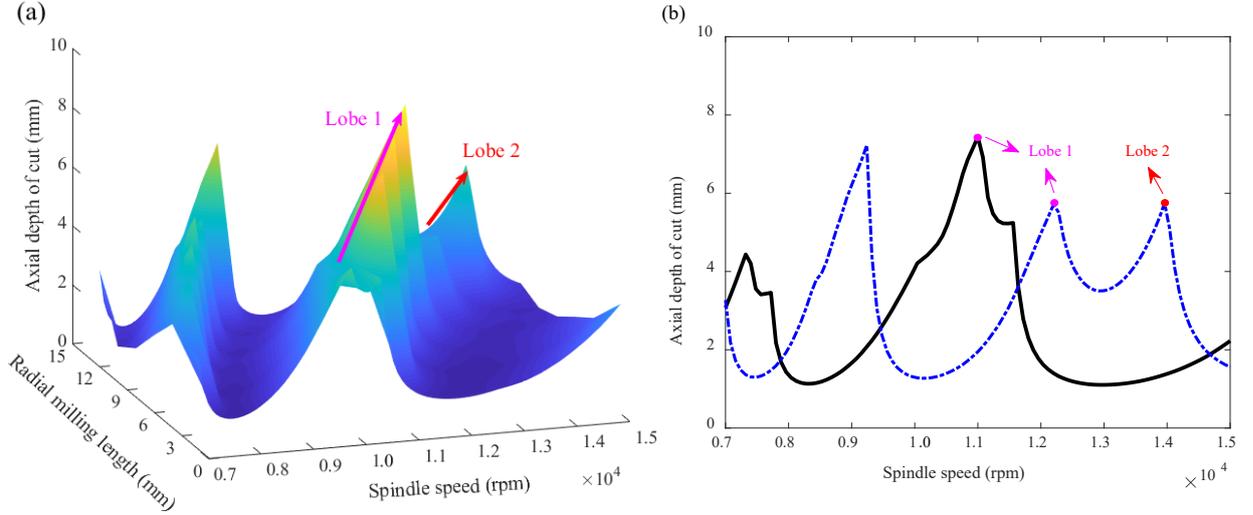
Figure 8. Conservative SLD and lobes distribution; (a) conservative 3D-SLD and its development trend without passive chatter suppression measures; (b) main lobe shift and distribution in the rage of 10000-15000 rpm. The black line shows the SLD at the radial milling length of 5 mm, and the blue line shows the SLD at the radial milling length of 11 mm.

Since changes in the natural frequency can cause a horizontal shift for the stability lobes, different machining stages correspond to different lobes. As depicted in Figures 8(a) and (b), Lobe 1 is the main lobe and it runs through the whole machining process in the range of 10000-15000 rpm. Lobe 2 appears slowly and starts to dominate the boundary when the radial milling length increases to 11 mm. In the range of 10000-15000 rpm, this 3D-SLD has the same development trend as the 3D-SLD constructed by the method presented in [65].

4.2. Workpiece FRF for passive chatter suppression measures

The stability enhancement relies on the stiffness of the machining system, i.e., the reduction of the FRF's amplitude and the increase of the natural frequency [54]. The structural dynamic modification method can be used to change the workpice FRF [69, 70], which affects the stability boundary. In the frequency domain, Eq. (12) can be written as:

$$\mathbf{F}(\omega) = \mathbf{B_0}(\omega)\mathbf{q_0}(\omega), \tag{21}$$

where $\mathbf{B_0}(\omega) = \mathbf{H_0^{-1}}(\omega)$, $\mathbf{H_0}(\omega)$ is the FRF of the original structure, $\mathbf{F}(\omega)$ is the external excitation and $\mathbf{q_0}(\omega)$ is the corresponding displacement of the original structure. When the local structural modification of the workpiece is applied, the dynamic modification matrix can be expressed as:

$$\Delta\mathbf{B}(\omega) = \Delta\mathbf{K} + i\omega\Delta\mathbf{C} - \omega^2\Delta\mathbf{M}, \tag{22}$$

where ΔK, ΔC and ΔM are stiffness modification matrix, damping modification matrix and mass modification matrix, respectively. Now Eq. (21) can be further developed as:

$$F(\omega) = [B_0(\omega) + \Delta B(\omega)] \; q_u(\omega), \tag{23}$$

where $q_u(\omega)$ is the response displacement of the updated modified structure. By multiplying Eq. (23) by $H_0(\omega)$, Eq. (23) becomes:

$$H_0(\omega)F(\omega) = H_0(\omega)[B_0(\omega) + \Delta B(\omega)] \; q_u(\omega) = [I + H_0(\omega)\Delta B(\omega)]q_u(\omega), \tag{24}$$

and consequently the FRF of the updated modified structure reads as:

$$H_u(\omega) = \frac{q_u(\omega)}{F(\omega)} = [I + H_0(\omega)\Delta B(\omega)]^{-1}H_0(\omega). \tag{25}$$

As the passive chatter suppression measures are imposed on Substructure B being the basis for subsequent coupling analysis, the unmodified Substructure B is regarded as the FRF original structure. Therefore, the FRF of the updated modified structure can be written as:

$$H_u(\omega) = \frac{H_0(\omega)}{1 + H_0(\omega)\Delta B(\omega)} \; . \tag{26}$$
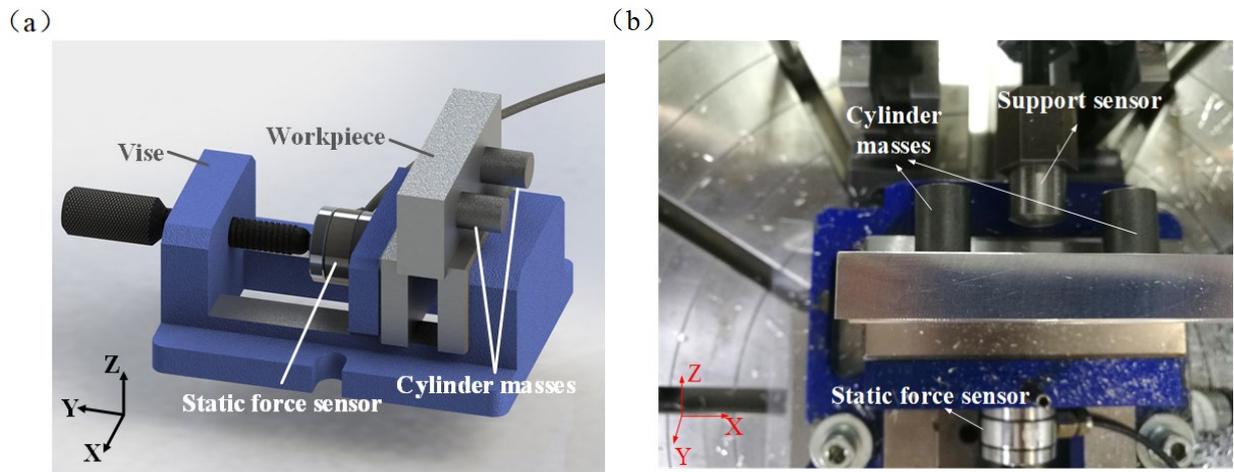
Figure 9. Milling experiment with additional cylinder masses applied to workpiece; (a) 3D model of the workpiece with additional cylinder masses; (b) experimental setup of the workpiece with additional cylinder masses. The two cylinder masses are symmetrically positioned on the workpiece and the clamping force was kept at 3000 N.

It can be seen from Eqs (26) and (22) that the updated FRF is mainly affected by the mass and stiffness modifications when the damping effect is neglected. In order to explore practical strategies for improving the stability of machining system, the FRF of the workpiece was investigated with two passive chatter suppression measures in form of additional cylinder masses and a passive support. As depicted in Figure 9, two cylinder

masses having diameter of 15 mm and length of 20 mm are symmetrically positioned on the workpiece and the material is a typical carbon steel C45. As the cylinder masses are much smaller than the workpiece pass, it is assumed that the natural frequency of the workpiece remains unchanged. Hence, Eq. (22) becomes $\Delta \mathbf{B}(\boldsymbol{\omega}) = -\boldsymbol{\omega}^2 \Delta \mathbf{M}$ and in this case, the real part of $\mathbf{H_0}(\boldsymbol{\omega})$ is 0 at the natural frequency, and the imaginary part corresponds to the negative resonance amplitude $(-\frac{1}{2\zeta_0 K_0})$. The updated FRF can be expressed as follows:

$$\text{Im }(\mathbf{H_u}(\omega_n)) = \frac{\text{Im }(\mathbf{H_0}(\omega_n))}{1 - \text{Im }(\mathbf{H_0}(\omega_n))\omega_n^2 \Delta \mathbf{M}} = -\frac{1}{2\zeta_0 K_0 + \omega_n^2 \Delta \mathbf{M}} \, , \tag{27}$$

where ζ_0 and K_0 are the damping ratio and stiffness matrix of the original structure. As $\text{Im }(\mathbf{H_u}(\omega_n)) > \text{Im }(\mathbf{H_0}(\omega_n))$, which indicates that the workpiece stiffness is increased after the cylinder masses are applied.

(a)   (b)
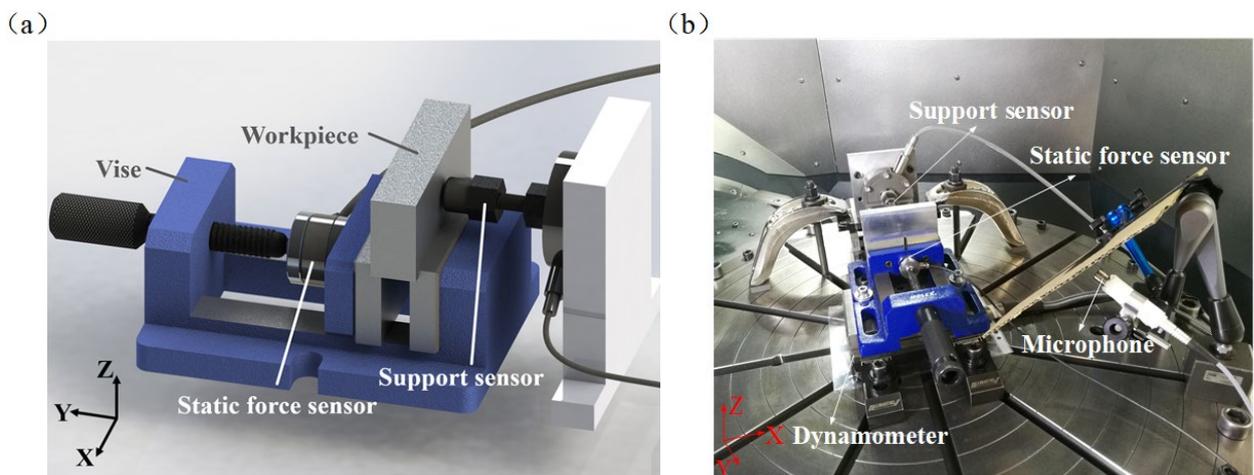
Figure 10. Milling experiments with the passive support; (a) schematic representation of the workpiece with the passive support; (b) experimental setup of the workpiece with the passive support sensor (GTM, Serie K-5kN). The passive support is applied at the center of the workpiece and the clamping force was kept at 3000 N.

The passive support force of 400 N was applied via the vice to the centre of the workpiece as shown in Figure 10, but the actual support force fluctuated between 404 and 416 N due to a contact gap between the support head and the workpiece. When the passive support is applied, according to Eq. (22) reduces to $\Delta \mathbf{B}(\omega) = \Delta \mathbf{K}$ as the dynamics components are zero. In this case, the imaginary part of $\mathbf{H_0}(\omega)$ is 0 at 0, and the real part corresponds to the compliance $(\frac{1}{K_0})$. Therefore, the updated FRF becomes:

$$\text{Re }(\mathbf{H_u}(0)) = \frac{\text{Re }(\mathbf{H_0}(0))}{1 + \text{Re }(\mathbf{H_0}(0))\Delta \mathbf{K}} = \frac{1}{K_0 + \Delta \mathbf{K}} \, . \tag{28}$$

Again as $\text{Re }(\mathbf{H_u}(0)) < \text{Re }(\mathbf{H_0}(0))$, the stiffness is higher, which also leads to an increase of the modified natural frequency.

In order to validate the above analysis, the impact hammer tests were carried out to the check the region T1 at

Stage 1, and the FRFs of the workpiece with and without chatter suppression measures are presented in Figure 11. As suspected both the frequency and amplitude of the workpiece decrease after attaching the cylinder masses, but the change in frequency was not significant when compared to the amplitude. The amplitude of the FRF decreased and the frequency increased after the passive support force was applied, and the changes of both were prominent. The amplitude of the FRF with passive support is smaller than that with cylinder masses, which indicates that the stiffness of the workpiece with the passive support is higher than that with the cylinder masses.
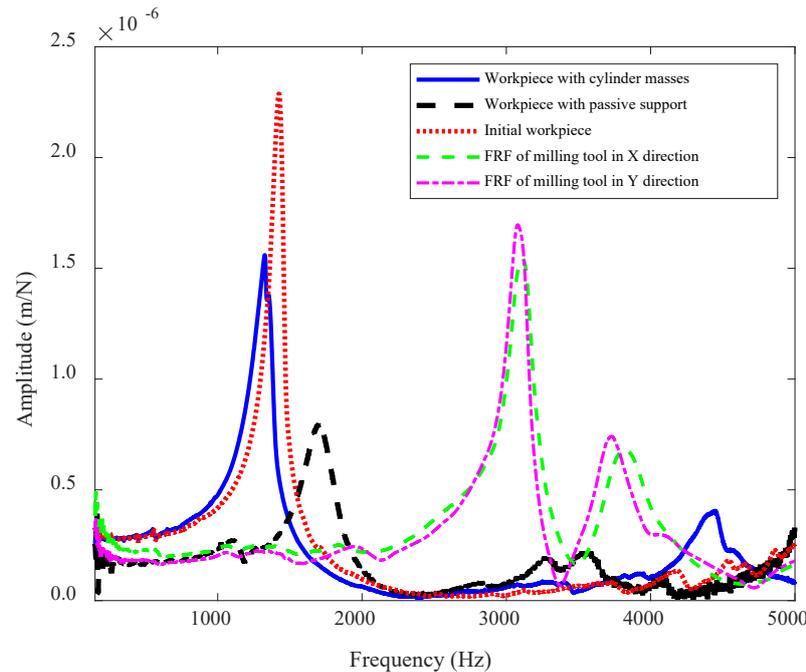
Fig. 11 FRFs comparison between the workpiece with and without cylinder masses. The blue line represents the FRF of workpiece with cylinder masses; the black line represents the FRF of workpiece with passive support; the red line represents the FRF of initial workpiece; the green line represents the FRF of milling tool in *X* direction; the pink line represents the FRF of milling tool in *Y* direction.

5. Milling experiments and discussion

From the dynamic tests shown in Figure 11, it can be deduced that the amplitude of the workpiece and the tool are basically in the same order of magnitude. Although the boundary of the conservative SLD is defined by the minimum stability limit, the milling tool may also dominate the machining process, and therefore, the SLD dominated by the milling tool is also used as an important reference. Whether the SLDs can be applied to practical milling processes needs to be validated by milling experiments. In addition, the effects of passive chatter suppression measures used in Section 4 also need validation. In this section, an experimental platform is introduced and the changes of cutting force and sound signal under different machining parameters are described

in detail in both time and frequency domains. Combined with the flowchart in Figure 7, the variation of the SLD and the dominant mode are analyzed.

5.1. Validation of SLD without and with passive chatter suppression measures

The SLD developed considering multiple modes of the machining system simultaneously is equivalent to the SLD that takes the lowest envelope of all single modes of the whole machining system separately, see [71] for details. In order to verify the excited modes in the SLD, Figure 8(a) is projected onto a two-dimensional coordinate system with the SLD induced by milling tool modes, and the minimum boundary of the system's stability is taken as the final conservative SLD to ensure the stability of continuous radial immersion milling process. Figure 12(a) shows the conservative 2D-SLD for the reference workpiece without any modifications. The maximum boundary of the SLD of the system does not exceed the SLD dominated by the milling tool, which indicates that the conservative 2D-SLD without modifications is dominated by the modal parameters of the workpiece.

(a)
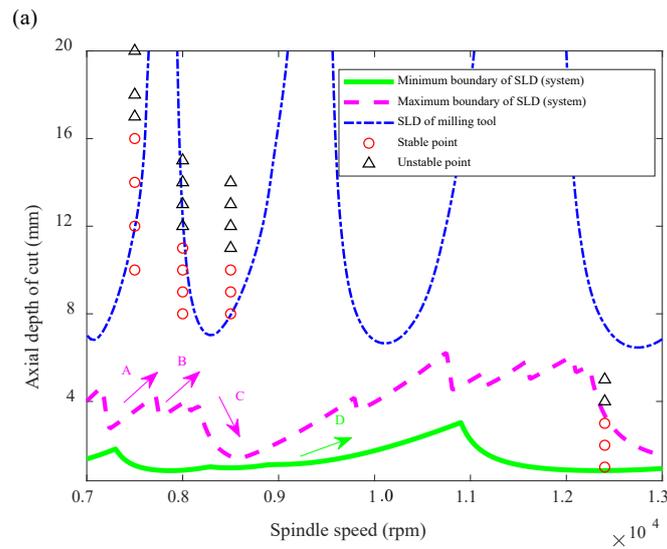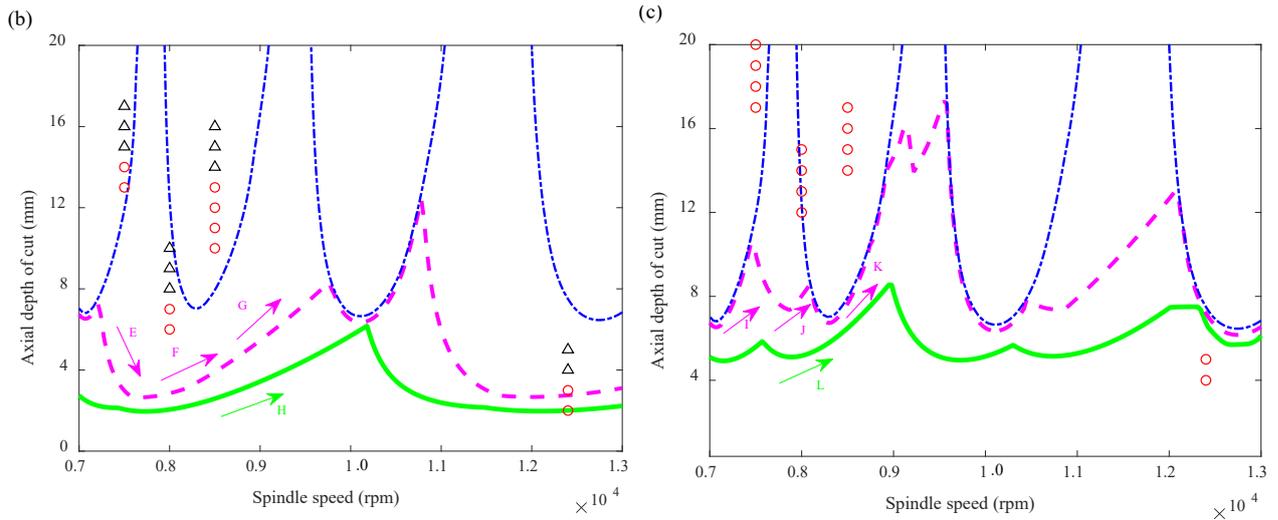
Figure 12. Comparison of SLDs for different scenarios; (a) conservative 2D-SLD without passive chatter suppression measures; (b) conservative 2D-SLD with cylinder masses attached to the workpiece; (c) conservative 2D-SLD with passive support applied to the workpiece. The blue curve represents the SLD of milling tool; the pink curve marks the maximum boundary of the SLD of machining system; the green curve represents the minimum boundary of the SLD of machining system. The circles and triangle mark stable and unstable machining responses respectively.

The spindle speeds at 7500 rpm, 8000 rpm, 8500 rpm and 12400 rpm were selected to conduct the cutting tests and Figure 10 shows the experimental passive support setup, where the clamping force was fixed to be 3000 N. The sound and dynamic force of the cutting process were recorded by a microphone and a dynamometer, which were used to determine whether the machining process was stable or not.
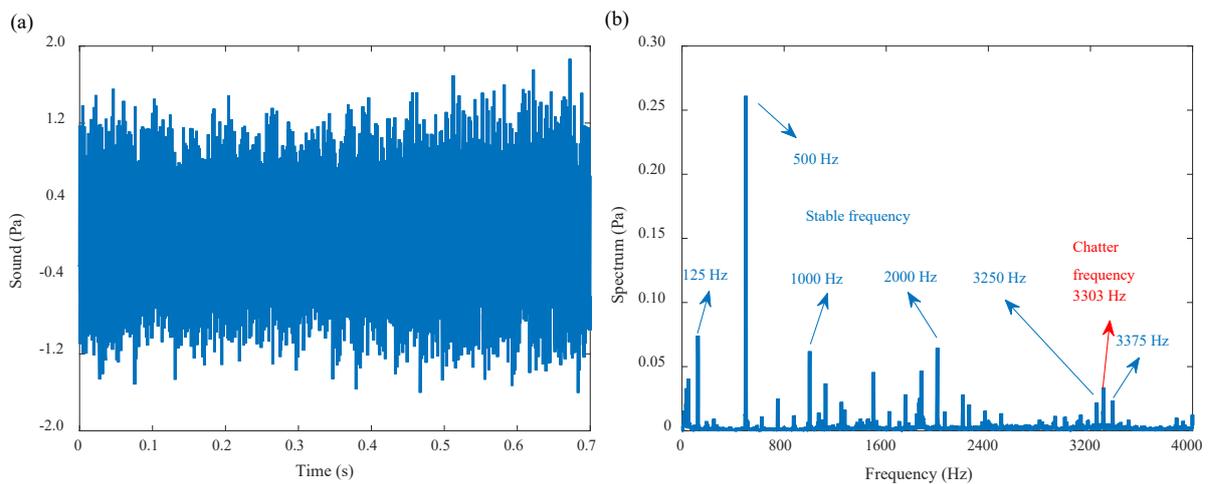
Figure 13. (a) Sound signal collected in time domain; (b) frequency analysis of the sound signal. The sound signal was collected at the spindle speed of 7500 rpm and axial depth of cut of 20 mm when the passive chatter suppression measures with no the passive chatter suppression measures. The fundamental and tooth passing frequencies were 125 and 500 Hz respectively.

Figure 13 shows the sound signal in the time domain at the speed of 7500 rpm (the spindle and tooth passing frequencies are 125 and 500 Hz) with the axial depth of cut of 20 mm, and slight fluctuations can be observed. As depicted in Figure 13(b), the chatter frequency of 3303 Hz was found in the sound signal spectrum, which was very close to the first mode natural frequency of the milling tool. To further verify the machining result, the surface topography of the machined workpiece was observed. As shown in Figure 14(a), there were obvious chatter marks in the machined surface topography. A similar verification of different machining parameters was shown in Figure 12(a). From the experimental results, it was clear that the machining process was closer to the SLD dominated by the dynamics of the milling tool at the spindle speeds of 7500 rpm, 8000 rpm and 8500 rpm, though the stiffness of the workpiece was lower. Therefore, the modes of the milling tool were excited instead of the workpiece.
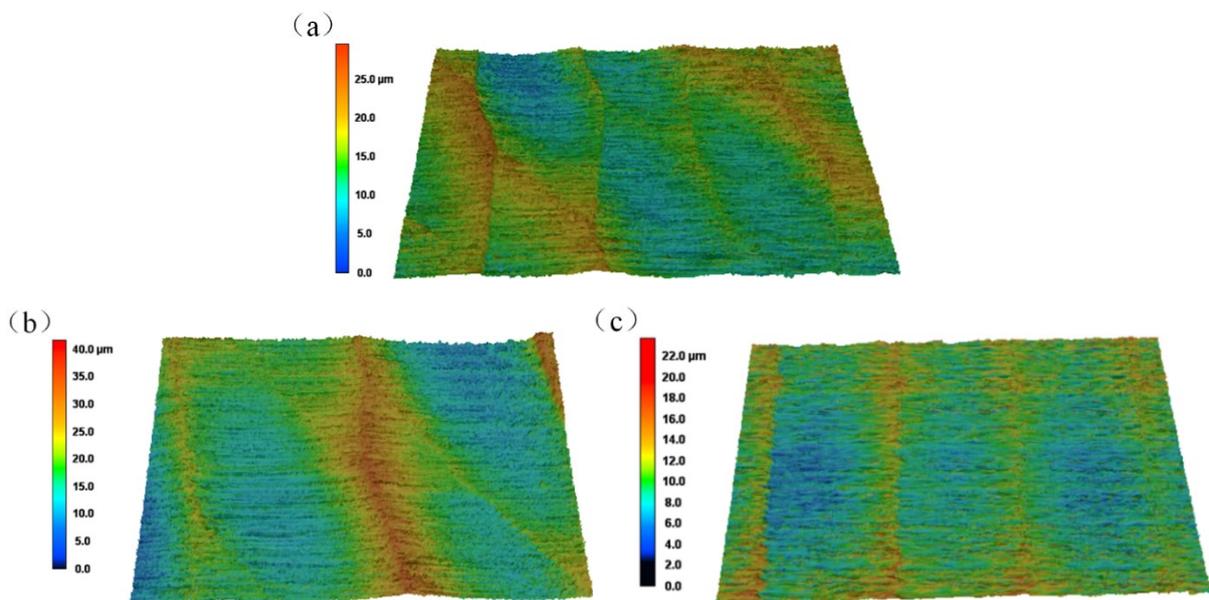
Figure 14. Surface topography of the workpiece measured by white light interferometer at different machining parameters; (a) workpiece without passive chatter suppression measures at the spindle speed of 7500 rpm and axial depth of cut of 20 mm; (b) workpiece without passive chatter suppression measures at the spindle speed of 12400 rpm and axial depth of cut of 5 mm; (c) workpiece with passive support at the spindle speed of 12400 rpm and axial depth of cut of 5 mm.

From Figure 12(a), it can be seen that the minimum stable depth of cut was 7 mm when the milling tool dominated the whole machining process. When the workpiece was continuously machined for 8 times with the spindle speed of 12400 rpm, which translates to the fundamental and tooth passing frequencies of 206.7 and 826.7 Hz, and axial depth of cut of 5 mm, severe chatter occurrences were observed. As shown in Figures 15(a) and 16(a), the cutting force tended to disperse and significant peaks appeared in the acoustic signals due to the occurrence of chatter.
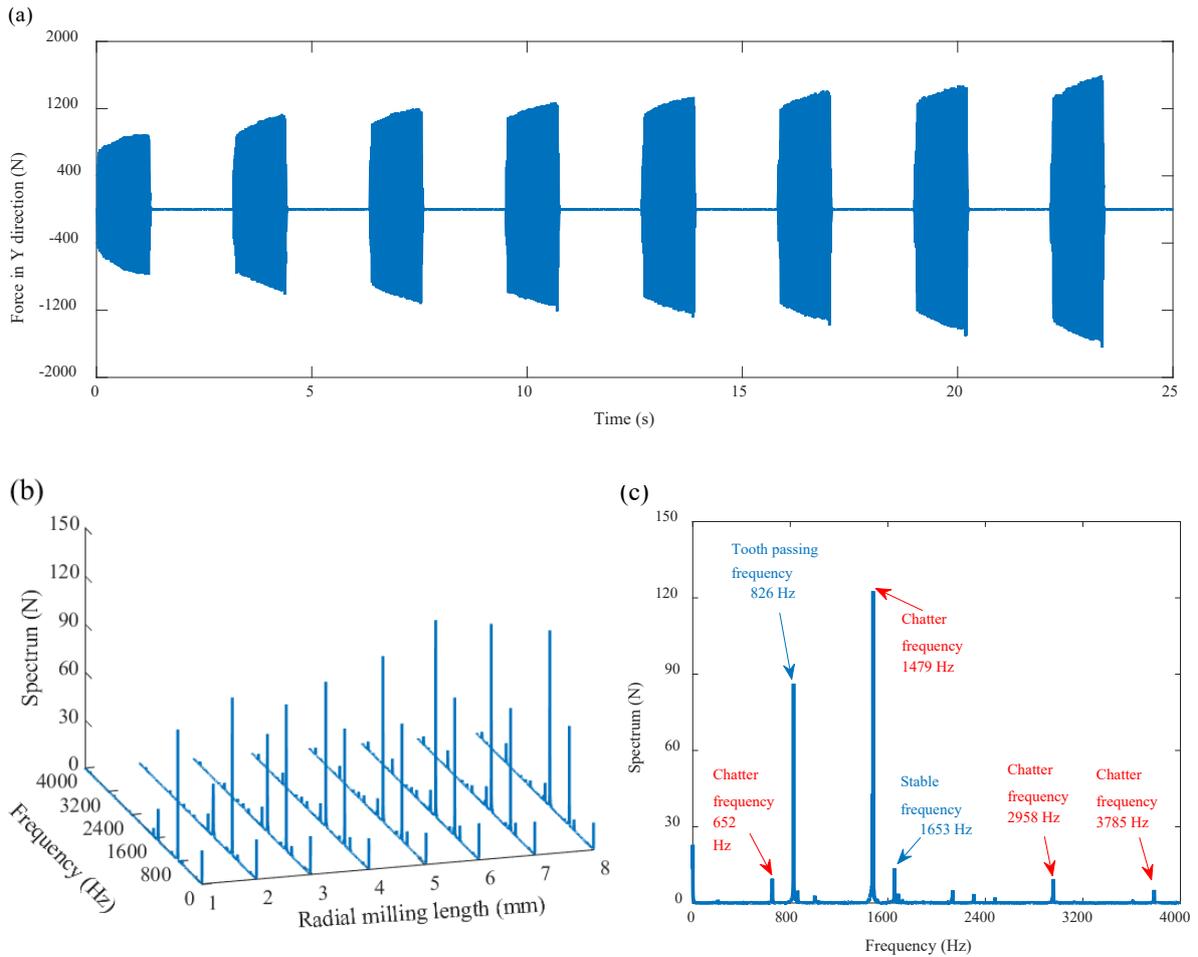
Figure 15. (a) Cutting force time history collected for 8 times immersion milling tests; (b) force spectrums of the 8 times immersion milling; (c) force spectrum at the sixth time immersion milling. The sound signal was collected at the spindle speed of 12400 rpm and axial depth of cut of 5 mm and with no the passive chatter suppression measures. The fundamental and tooth passing frequencies were 206.7 and 826.7 Hz respectively.

It can be seen from Figure 15(a) that the cutting force peak had gradually increased during the first radial immersion, which is a typical feature of chatter generation, indicating that the previous and current dynamic cutting thicknesses were out of phase. Accordingly, large fluctuations in dynamic cutting force appeared. When entering the next radial immersion, the phase relations were still unfavorable, so the chatter of each radial immersion had made the fluctuation of cutting force more and more intense. It can be seen from Figure 15(b) that the highest amplitude of chatter frequency at 1479 Hz had slowly increased from the first radial immersion, and this frequency ran through the whole machining process. The sound signal in Figure 16(a) was relatively gentle during the first radial immersion, and it gradually had showed larger fluctuations at the second radial immersion reaching the maximum value at the seventh radial immersion, which indicated that the influence of chatter was strengthened. The amplitude of chatter frequency at 1479 Hz in Figure 16(b) had shown a similar trend.
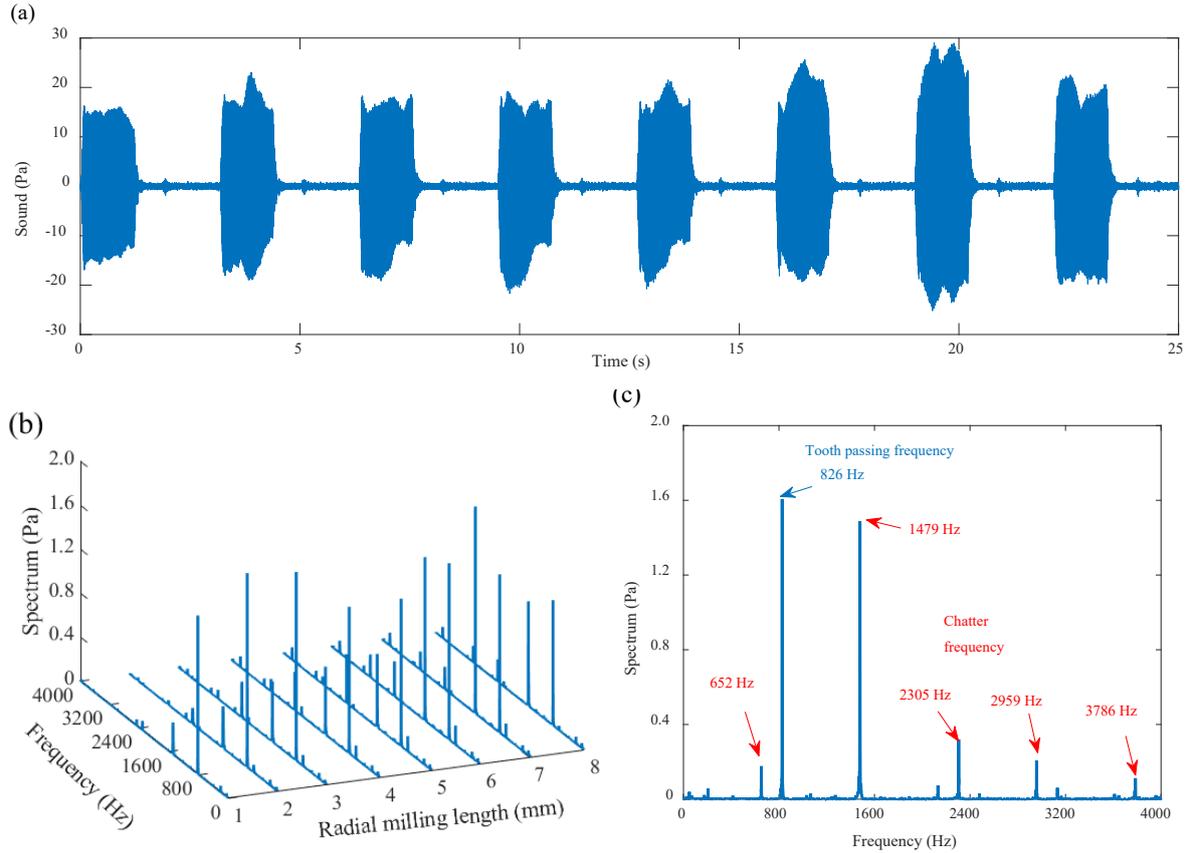
Figure 16. (a) Sound signal collected in time domain with 8 times immersion milling; (b) acoustic spectrums of the 8 times immersion milling; (c) acoustic spectrum at the sixth time immersion milling. The sound signal was collected at the spindle speed of 12400 rpm and axial depth of cut of 5 mm with no the passive chatter suppression measures. The fundamental and tooth passing frequencies were 206.7 and 826.7 Hz respectively.

As shown in Figures 15(c) and 16(c), the spectrums of the cutting force and sound signal in the frequency domain were calculated analyzed, and the chatter frequency of 1479 Hz was close to the natural frequency of the first mode of the workpiece. This meant the one of the workpiece modes was excited when machining with the spindle speed of 12400 rpm and axial depth of cut of 5 mm. After examining the surface topography of the machined workpiece shown in Figure 14(b), chatter marks were clearly visible.

The passive chatter suppression measures affect the contact state of Substructure B (see Figure 2) and does not affect the method used to extract the mode shapes presented in Section 2. As shown in Figure 12(b), the conservative 2D-SLD with cylinder masses is obtained according to the procedure presented in Figure 7. The maximum boundary of the system's SLD is limited by the boundary of the tool-dominated SLD. It means that the conservative 2D-SLD with cylinder masses is jointly determined by the modal parameters of the milling tool and workpiece. At this time, the machining process was still closer to the SLD dominated by the milling tool. However, the boundary of the SLD dominated by milling tool varied, which indicated that the cylinder masses not only

directly changed the dynamics of the workpiece, but also indirectly affected the dynamics of the milling tool. Therefore, during the contact interaction between the milling tool and workpiece, modifications of the workpiece could affect the dynamics of the milling tool through the contact zone. When the machining parameters with spindle speed of 12400 rpm, axial depth of cut of 5 mm, were selected for 8 times radial consecutive immersion, the whole machining process became unstable, which caused the cylinder masses to fall off. This further suggested that the resonant mode of workpiece played a dominant role for 8 times consecutive machining.
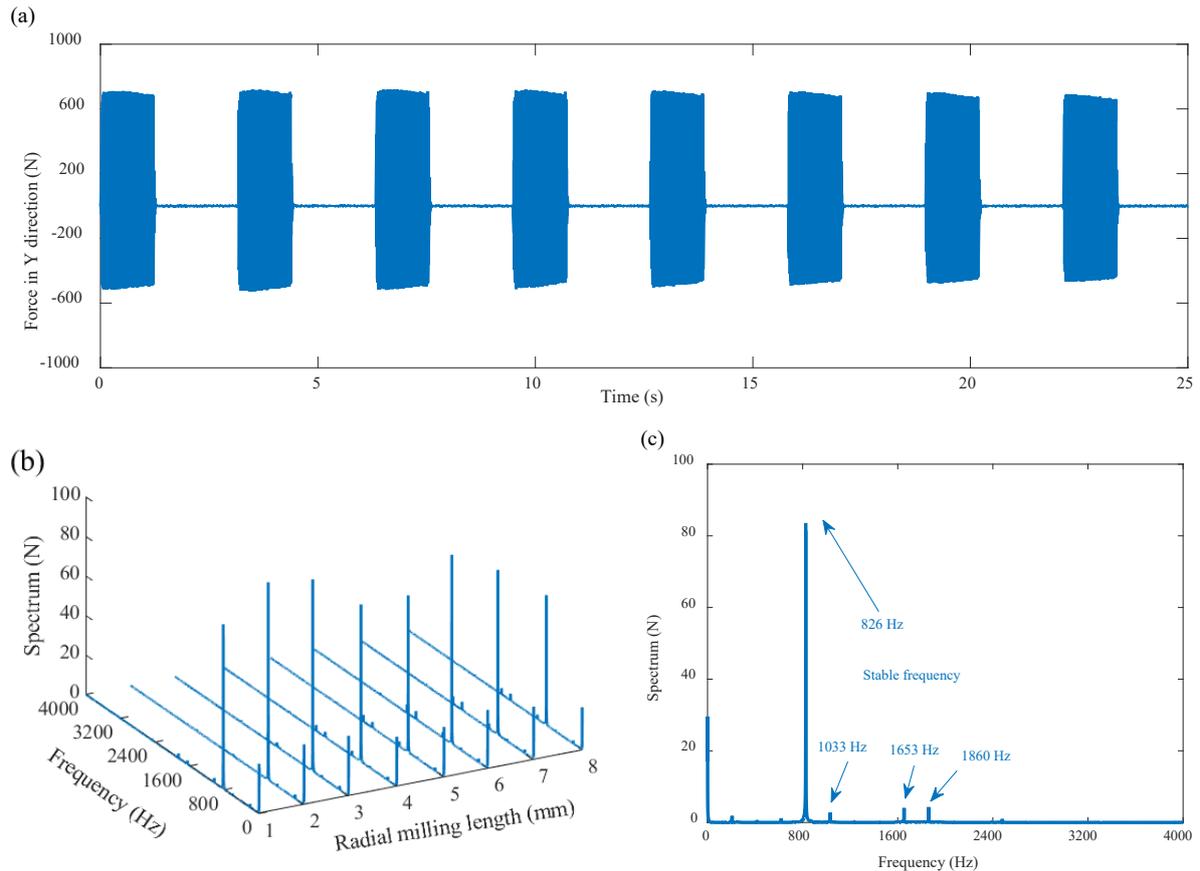
Figure 17. (a) Cutting force time history collected during 8 times immersion milling tests; (b) force spectrums of the 8 times immersion milling; (c) force spectrum at the sixth time immersion milling. The sound signal was collected at the spindle speed of 12400 rpm and axial depth of cut of 5 mm when the passive support was applied to the workpiece. The spindle and tooth passing frequencies were 206.7 and 826.7 Hz respectively.

Once the passive support was applied to the workpiece, the stability of the machining parameters had changed significantly. As shown in Figures 17(a) and 18(a), when the spindle speed of 12400 rpm and axial depth of cut of 5 mm were used for 8 times continuous radial immersion, the cutting force and the sound signal did not show significant fluctuations in the time domain. In Figures 17(b, c) and 18(b, c), there was no chatter signals in the frequency domain, which showed that the whole milling process was stable. As shown in Figure 14(c), there was no obvious chatter marks in the machined surface, and only the traces left by the tool feed can be found. Therefore,

chatter did not occur during this machining process. At this time, the stable responses shown in Figure 12(c) were still close to the SLD dominated by the milling tool, but the stability boundary seemed to change with the passive support applied.
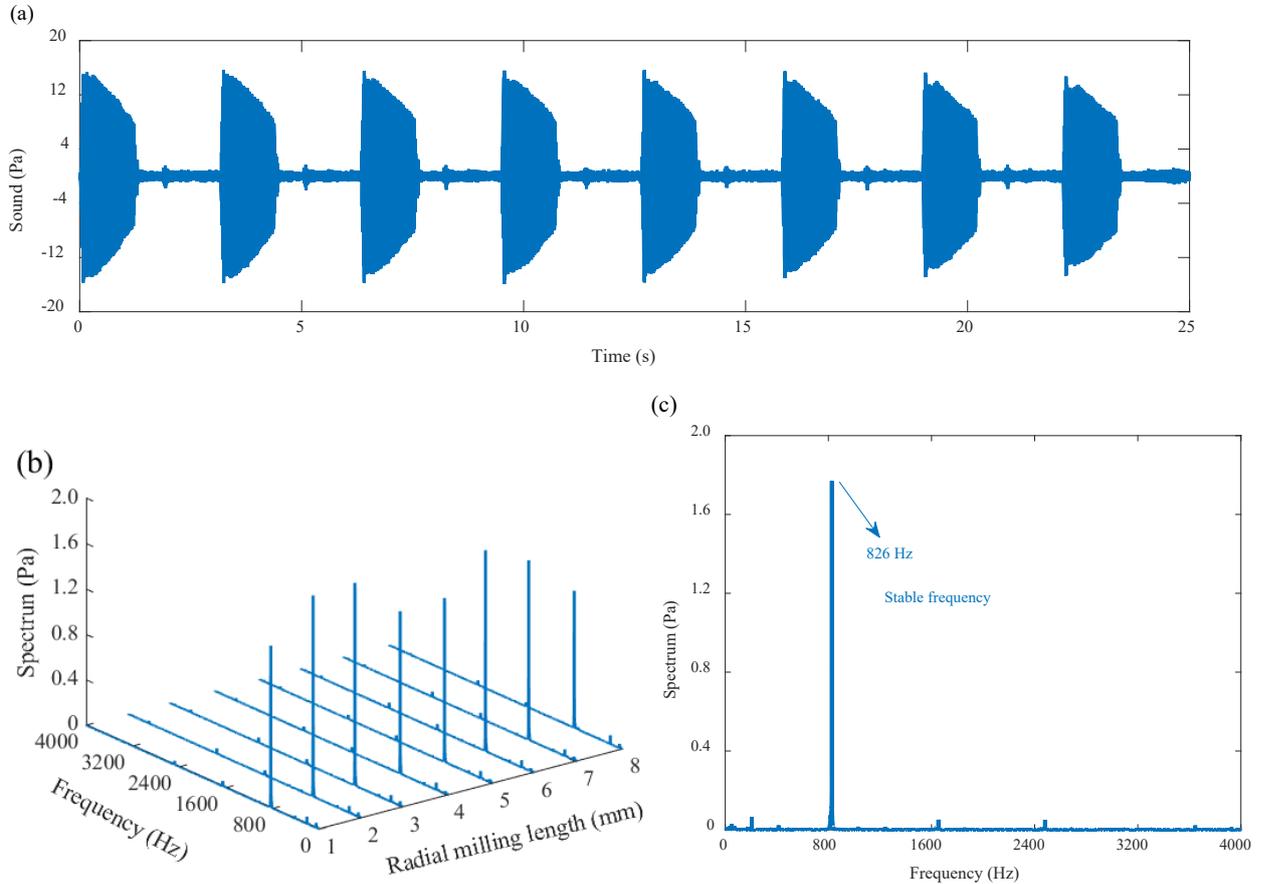

Figure 18. (a) Sound signal time history for 8 immersion milling tests; (b) acoustic spectrums of the 8 times immersion milling; (c) acoustic spectrum at the sixth time immersion milling. The sound signal was collected at the spindle speed of 12400 rpm and axial depth of cut of 5 mm when the passive support was applied to the workpiece. The spindle and tooth passing frequencies were 206.7 and 826.7 Hz respectively.

5.2. Discussion and analysis of the experiments

The main reason for the variation in the SLDs depicted in Figures 12(b) and (c) is the mass-normalized mode shape and frequency change when the passive chatter suppression measures are applied, i.e., the change in the FRFs. The FRFs of the workpiece with cylinder masses and passive support are calculated and fitted according to the methodology presented in Section 2 and 3, as shown in Figure 19. From Figures 5 and 6, it can be seen that the variation of mass-normalized mode shapes is small, while the change of natural frequency is relatively large and Figure 19 exhibits also a similar trend. The FRFs in Figure 5 corresponds to Figure 12(a), and the two sets of FRFs in Figure 19 correspond to Figures 12(b) and 12(c) respectively. From the results in Figure 19, the

amplitudes of the FRFs are reduced, so the mass-normalized mode shapes are also decreased, especially for the workpiece with the passive support. The decrease of mass-normalized mode shape and the increase of natural frequency, make an improvement in the stability limit of the workpiece for the passive support case more evident.
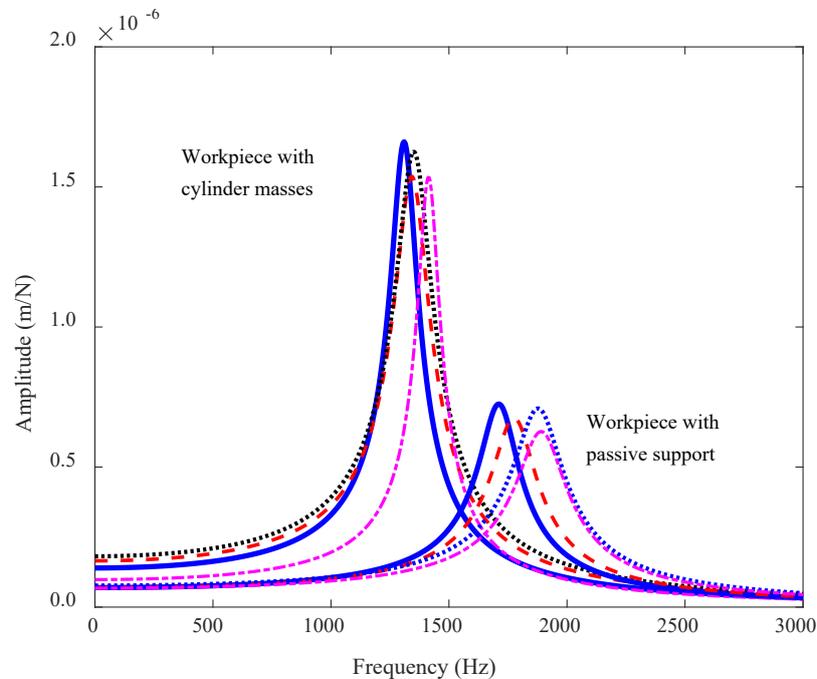

Figure 19. FRFs with passive chatter suppression measures applied to workpiece at different machining stages. There are two groups of FRFs: one is the workpiece with cylinder masses (1312 Hz→1346 Hz→1355 Hz→1415 Hz), and the other is the workpiece with passive support (1715 Hz→1780 Hz→1883 Hz→1896 Hz). The blue curve marks the FRF of the workpiece at Stage 1; the red curve depicts the FRF of the workpiece at Stage 2; the black curve represent the FRF of the workpiece at Stage 3; the pink curve marks the FRF of the workpiece at Stage 4.

For the SLD without passive chatter suppression measures in Figure 12(a), when the milling tool dominates the machining process at the spindle speed of 7500 rpm, 8000rpm and 8500 rpm, the maximum stability limit of the system shows three small increasing trends (Arrow A, Arrow B and Arrow C). The minimum stability limit of the system shows a slow increasing trend (Arrow D). For the SLD with cylinder masses in Figure 12(b), the maximum stability limit of the system is located at the bottom of the lobe at the spindle speed of 7500 rpm and 8000rpm, and shows a large decreasing trend (Arrow E and Arrow F); while the maximum boundary and the minimum boundary of the SLD at the spindle speed of 8500 rpm are in an obvious upward stage (Arrow F, Arrow G and Arrow H). It can be found that the stability limit decreases from 16 mm to 14 mm at 7500 rpm and from 11 mm to 7 mm at 8000 rpm. However, the stability limit increases from 10 mm to 13 mm at 8500 rpm. Although the

stability limit corresponding to the above spindle speeds is very close to the dominant mode of the milling tool, it is clear that the trend of the stability boundaries o also affects the stability of the selected machining parameters. For the SLD with passive support in Figure 12(c), the maximum and minimum stability limits of the system show an increasing trend at the above spindle speeds (Arrow I, Arrow J, Arrow K and Arrow L), and the unstable machining parameters in Figure 12(a) become stable from the experimental results. Compared with the conservative SLD without the passive chatter suppression measures, it can be seen that both passive chatter suppression measures improve the boundary of the conservative SLDs. The stability limit of the conservative SLD without suppression measures is about 1.5 mm, and it increases to 2.2 mm after adding additional cylinder masses. When the passive support is applied, the stability limit grows to 5.3mm. Obviously, the boundary of conservative SLD with the passive support is significantly higher than that with cylinder masses, which further indicates the modification effect of passive support is better than that with additional cylinder masses. Therefore, modifications to the passive support can be preferentially used to suppress chatter during continuous radial immersion milling.

The experimental results presented in Section 5.1 indicate that when the system stability boundary shows a downward trend, it can reduce the stability limit dominated by the tool mode, and when the system stability boundary shows an upward trend, it can increase the stability limit dominated by the tool mode. When the workpiece dominates the whole machining process, there is a maximum and minimum boundary for the stability limit of the system. As the maximum boundary does not necessarily satisfy all machining stages, and using the maximum stability limit of the system still faces a risk of inaccurate predictions shown in Figures 12(a) and (b), obtained at the spindle speed of 12400 rpm and axial depth of cut of 4 and 3 mm. Therefore, the minimum limit of the system's SLD is selected as the conservative SLD. Due to the influence of rotating speeds and tool-workpiece contact interactions, the modal parameters of the milling tool obtained under static conditions change during the cutting process. When the passive chatter suppression measures are applied to the workpiece, the influence of the tool-workpiece contact on the tool-dominated SLD is more significant. From the experimental results, the passive chatter suppression measures applied to the workpiece also affect the dynamic response of the milling tool.

Stability predictions for continuous machining processes is only one of the important means to ensure stability. It is not the first choice to ensure the stability only through the selection of machining parameters. The ultimate goal of cutting process is to ensure the machining quality and improve the machining efficiency as much as possible. An increase of the stiffness can not only prevent the occurrence of chatter, but also improve the

machining efficiency indirectly. Therefore, a right combination of the machining and system parameters, especially the stiffness, is a key to achieve high cutting performance. It is clear from the carried out experiments that determination of the time-varying modal parameters during the continuous radial immersion needs to be analyzed in a specific clamping state. Undertaking a programme of dynamic tests is particularly important, when the workpiece is flexibly clamped, and these results can provide practical modal parameters to construct SLDs. During continuous material removal process, there are also cases where the flexibility of workpiece is not very different from the flexibility of tool, and therefore the dominant mode of the machining system changes. In essence, the chatter can be effectively avoided by using conservative SLDs. To further enhance the boundary of the SLD, the workpiece is modified to improve its stiffness, which is also an effective measure to ensure stability for continuous radial immersion milling operations.

6. Conclusions

In this paper, a new method for rapid acquisition of workpiece mode shapes in continuous radial immersion milling is proposed, which combines the mass-normalized mode shapes and receptance coupling. The Timoshenko beam model was applied to simulate the dynamics of the workpiece, however in general, for very thin-walled workpieces shell theory can be advantageous. In addition, we developed an experimental rig for measuring and adjusting the clamping force between the workpiece and the vise and through the experimental identification was employed to obtain the dynamic coupling matrix between workpiece and vise. Finally, the time-varying frequencies and mode shapes under different machining stages were obtained, which shortened the time for the creation of the conservative SLD and provided a theoretical basis for continuous stable radial immersion milling. Based on the proposed method, the conservative SLDs for the cases of additional cylinder masses and passive support were investigated separately and verified by dedicated cutting experiments.

The paper focuses on the continuous radial immersion milling process for general shape workpiece, in which the thickness of the workpiece is gradually reduced. A thin-walled workpiece is the main feature of the continuous radial immersion milling process, so the method is applicable for other machining operations of thin-walled workpieces. For large and typical shape workpieces, the proposed method has extra advantages due to its ability to obtain the modal parameters of workpiece for different machining stages. For smooth surfaces with moderate curvature changes, the time-varying modal parameters can be obtained by this method, however for the

complex surfaces, the FRF of substructure is difficult to calculate due to demanding discretization and difficulties in simplifying cross-sectional areas.

As the FRFs of the workpiece change with respect to the clamping forces, the measured dynamics are employed to identify the dynamic coupling matrix and the FRF of the workpiece in the real clamping state can be determined. Compared with the test results, the flexible-damped coupling model with the dynamic coupling matrix can effectively predict the workpiece FRF under a chosen clamping condition, which lays the foundations for an accurate extraction of the modal parameters. When the milling tool-workpiece system has a little difference in stiffness, the modes with lower stiffness under static test are not always excited. As a result, the conservative SLD varied with radial milling length does not necessarily accurately accord with the real machining process. Although the material removal rate is reduced, the minimum boundary of the conservative SLD ensures the stability of the entire machining process. For the passive chatter suppression, both measures with the additional cylinder masses and passive support were effective for improving the minimum boundary of the conservative SLD, and the passive support worked better.

For the machining system that is difficult to determine a relative stiffness between the workpiece and tool, it is difficult to determine which mode of the system will be excited. The modal parameters of the system during machining process are time-varying and the SLD of the system changes, which is the main reason why the SLD is difficult to be widely used in practice. When the vibration modes during machining are transferred between the milling tool and workpiece, the mode transition mechanism is yet to be unveiled.

Authorship contribution

Dongqian Wang: Methodology; Investigation; Conceptualization; Validation; Visualization; Writing - original draft.

Lars Penter: Project administration; Investigation; Writing - reviews & editing.

Albrecht Hänel: Methodology; Validation; Data collection; Analysis.

Steffen Ihlenfeldt: Idea suggestion; Investigation; Supervision; Resources; Funding acquisition.

Marian Wiercigroch: Review of modelling and analysis; Writing – reviews.

Declaration of Competing Interest

No conflicts of interest exist in the submission of this manuscript.

Acknowledgments

References

[1] Yan BL, Hao YP, Zhu LD, Liu CF. Towards high milling accuracy of turbine blades: A review. Mech Syst Signal Proc. 2022;170:108727.

[2] Altintas Y, Budak E. Analytical prediction of stability lobes in milling. Annals of CIRP. 1995;44(1):357-362.

[3] Tunc LT, Budak E. Identification and modeling of process damping in milling. J. Manuf. Sci. Eng. 2013;135(2):021001-1-021001-12.

[4] Tyler CT, Schmitz TL. Analytical process damping stability prediction. J. Manuf. Process. 2013:15:69–76.

[5] Niu JB, Ding Y, Zhu LM, Ding H. Mechanics and multi-regenerative stability of variable pitch and variable helix milling tools considering runout. Int J Mach Tools Manuf. 2017;123:129-145.

[6] Zhang XJ, Xiong CH, Ding Y, Feng MJ, Xiong YL. Milling stability analysis with simultaneously considering the structural mode coupling effect and regenerative effect. Int J Mach Tools Manuf. 2012;53:127-140.

[7] Ji YJ, Wang XB, Liu ZB, Wang HJ, Jiao L, Zhang L, Huang T. Milling stability prediction with simultaneously considering the multiple factors coupling effects-regenerative effect, mode coupling, and process damping. Int J Adv Manuf Technol. 2018;97:2509-2527.

[8] Sun YW, Jiang SL. Predictive modeling of chatter stability considering force-induced deformation effect in milling thin-walled parts. Int J Mach Tools Manuf. 2018;135:38-52.

[9] Urbikain G, Olvera D, Lacalle LNL. Stability contour maps with barrel cutters considering the tool orientation. Int J Adv Manuf Technol. 2017; 89:2491–2501.

[10] Wang DZ, Ren JX, Tian WJ. Influences of modal shape and tool orientation on evolution of dynamic responses in 5-axis milling of thin-walled parts. Int J Adv Manuf Technol. 2022;119:4485-4508.

[11] Bachrathy D, Stépán G, Turi J. State dependent regenerative effect in milling processes. J Comput Nonlinear Dynam 2011;6:041002-1-041002-9.

[12] Ding Y, Zhu LM, Zhang XJ, Ding H. A full-discretization method for prediction of milling stability. Int J Mach Tools Manuf. 2010;50:502-509.

[13] Insperger T, Munoa J, Zatarain M, Peigne G. Unstable islands in the stability chart of milling processes due to the helix angle. In: CIRP 2nd international conference on high performance cutting, Vancouver, Canada; 2006. p. 1-10.

[14] Grossi N, Sallese L, Scippa A, Campatelli G. Speed-varying cutting force coefficient identification in milling. Precis Eng. 2015;42:321-334.

[15] Grossi N, Sallese L, Scippa A, Campatelli G. Improved experimental-analytical approach to compute speed-varying tool-tip FRF. Precis. Eng 2017;48:114-122.

[16] Wan M, Dong ZY, Yang Y, Zhang WH. Stability analysis of milling process by combining the gyroscopic effect with the symmetry and runout of the cutter. Mech Syst Signal Proc. 2021;161:107977.

[17] Molnar TG, Insperger T, Bachrathy D, Stepan G. Extension of process damping to milling with low radial immersion. Int J Adv Manuf Technol. 2017;89:2545–2556.

[18] Zhang XM, Zhu LM, Zhang D, Ding H, Xiong YL. Numerical robust optimization of spindle speed for milling process with uncertainties. Int J Mach Tools Manuf. 2012;61:9-19.

[19] Löser M, Otto A, Ihlenfeldt S, Radons G. Chatter prediction for uncertain parameters, Adv. Manuf. 2018;6:319-333.

[20] Wu G, Li GX, Pan WC, Raja I, Wang X, Ding SL. A state-of-art review on chatter and geometric errors in thin-wall machining processes. J. Manuf. Process. 2021;68:454-480.

[21] Filho JMC, Negri D, Melotti S. Stable milling of cantilever plates using shell finite elements. Int J Adv Manuf Technol. 2018;99(9–12):2677–2693.

[22] Wang DZ, Ren JX, Tian WJ, Shi KN, Zhang BG. Predicting the dynamics of thin-walled parts with curved surfaces in milling based on FEM and Taylor series. Int J Adv Manuf Technol. 2019;103:927-942.

[23] Nikolaev S, Kiselev I, Kuts V, Voronov S. Optimal milling modes identification of a jet-engine blade using time-domain technique. Int J Adv Manuf Technol. 2020;107:1983–1992.

[24] Song QH, Liu ZQ, Wan Y, Ju GG, Shi JH. Application of Sherman-Morrison-Woodbury Formulas in Instantaneous Dynamic of Peripheral Milling for Thin-Walled Component. Int J Mech Sci. 2015;96-97:79-90.

[25] Tuysuz O, Altintas Y. Frequency domain updating of thin-walled workpiece dynamics using reduced order substructuring method in machining. Manuf Sci Eng. 2017;139:071013-1–071013-16.

[26] Tuysuz O, Altintas Y. Time-domain modeling of varying dynamic characteristics in thin-wall machining using perturbation and reduced-order substructuring methods. J Manuf Sci Eng. 2018;140:011015-1-011015-15.

[27] Hamann D, Eberhard P. Stability analysis of milling processes with varying workpiece dynamics. Multibody Syst Dyn 2018;42:383–396.

[28] Dang XB, Wan M, Yang Y, Zhang WH. Efficient prediction of varying dynamic characteristics in thin-wall milling using freedom and mode reduction methods. Int J Mech Sci. 2019;150:202-216.

[29] Yang Y, Zhang WH, Ma YC, Wan M, Dang XB. An efficient decomposition-condensation method for chatter prediction in milling large-scale thin-walled structures. Mech Syst Signal Proc. 2019;121:58-76.

[30] Li WT, Wang LP, Yu G, Wang D. Time-varying dynamics updating method for chatter prediction in thin-walled part milling process. Mech Syst Signal Proc. 2021;159:107840.

[31] Karimi B, Altintas Y. Hybrid modeling of position dependent dynamics of thin-walled parts using shell elements for milling simulation. J Manuf Sci Eng. 2022; https://doi.org/10.1115/1.4053596.

[32] Honeycutt A, Schmitz T. Receptance coupling model for variable dynamics in fixed-free thin rib machining. Procedia Manufacturing, 2018;26:173-180.

[33] Zhu LD, Liu CF. Recent progress of chatter prediction, detection and suppression in milling. Mech Syst Signal Proc. 2020;143:106840.

[34] Luo M, Luo H, Axinte D, Liu DS, Mei JW, Liao ZR. A wireless instrumented milling cutter system with embedded PVDF sensors. Mech Syst Signal Proc. 2018;110:556–568.

[35] Ji YJ, Wang XB, Liu ZB, Wang HJ, Jiao L, Wang DQ, Leng SY. Early milling chatter identification by improved empirical mode decomposition and multi-indicator synthetic evaluation. J. Sound Vibr. 2018;433:138-159.

[36] Cao L, Zhang XM, Huang T, Zhang XJ, Ding H. An adaptive chatter signal enhancement approach for early fault diagnosis in machining process. Procedia CIRP. 2019;82:308–313.

[37] Kalinski KJ, Galewski MA. Vibration surveillance supported by Hardware-In-the-Loop Simulation in milling flexible workpieces. Mechatronics. 2014;24:1071-1082.

[38] Rafal R, Pawel L, Krzysztof K, Bogdan K, Jerzy W. Chatter identification methods on the basis of time series measured during titanium superalloy milling. Int J Mech Sci. 2015;99:196-207.

[39] Caliskan H, Kilic ZM, Altintas Y. On-line energy-based milling chatter detection. J. Manuf. Sci. Eng. 2018;140:111012.

[40] Liu CF, Zhu LD, Ni CB. Chatter detection in milling process based on VMD and energy entropy. Mech Syst Signal Proc. 2018;105:169-182.

[41] Li K, He SP, Li B, Liu HQ, Mao XY, Shi CM. A novel online chatter detection method in milling process based on multiscale entropy and gradient tree boosting. Mech Syst Signal Proc. 2020;135:106385.

[42] Munoa J, Beudaert B, Dombovari Z, Altintas Y, Budak E, Brecher C, Stepan G. Chatter suppression techniques in metal cutting. CIRP Ann-Manuf. Technol. 2016;65:785-808.

[43] Smis ND. Vibration absorbers for chatter suppression: A new analytical tuning methodology. J. Sound Vibr. 2007;592-607.

[44] Miguelez MH, Rubio L, Loya JA, Fernandez-Saez L. Improvement of chatter stability in boring operations with passive vibration absorbers. Int J Mech Sci. 2010;52:1376-1384.

[45] Yang YQ, Munoa J, Altintas Y. Optimization of multiple tuned mass dampers to suppress machine tool chatter. Int J Mach Tools Manuf. 2010;50:834-842.

[46] Munoa J, Mancisidor I, Loix N, Uriarte L, Barcena R, Zatarain M. Chatter suppression in ram type travelling column milling machines using a biaxial inertial actuator. CIRP Ann-Manuf. Technol. 2013;62:407-410.

[47] Munoa J, Beudaert X, Erkorkmaz K, Iglesias A, Barrios A, Zatarain M. Active suppression of structural chatter vibrations using machine drives and accelerometers. CIRP Ann-Manuf. Technol. 2015;64:385-388.

[48] Totis G, Albertelli P, Sortino M, Monno, M. Efficient evaluation of process stability in milling with spindle speed variation by using the Chebyshev collocation method. J. Sound Vibr. 2014;333:646-668.

[49] Yamato S, Ito T, Matsuzaki H, Kakinuma Y, Programmable optimal design of sinusoidal spindle speed variation for regenerative chatter suppression. Procedia manufacturing. 2018;18:152-160.

[50] Fei JX, Lin B, Yan S, Ding M, Xiao JL, Zhang J, Zhang XF, Ji CH, Sui TY. Chatter mitigation using moving damper. J. Sound Vibr. 2017;410:49-63.

[51] Zhang Z, Li HG, Meng G, Ren S. Milling chatter suppression in viscous fluid: A feasibility study. Int J Mach Tools Manuf. 2017;120:20-26.

[52] Zhang Z, Liu HG, Liu XB, Zhang WY, Meng G. Chatter mitigation for the milling of thin-walled workpiece. Int J Mech Sci. 2018;138-139:105543.

[53] Wan M, Dang XB, Zhang WH, Yang Y. Optimization and improvement of stable processing condition by attaching additional masses for milling of thin-walled workpiece. Mech Syst Signal Proc. 2018;103(1):196-215.

[54] Wan M, Gao TQ, Feng J, Zhang WH. On improving chatter stability of thin-wall milling by prestressing. J. Mater. Process. Technol. 2019;264:32-44.

[55] Liu Y, Liu ZQ, Song QH, Wang B. Development of constrained layer damping toolholder to improve chatter stability in end milling. Int J Mech Sci. 2016;117:299-308.

[56] Gibbons TJ, Ozturk E, Xu LJ, Sims ND. Chatter avoidance via structural modification of tool-holder geometry. Int J Mach Tools Manuf. 2020, 150:103514.

[57] Munoa J, Sanz-Calle M, Dombovari Z, Iglesias A, Pena-Barrio J, Stepan G. Tuneable clamping table for chatter avoidance in thin-walled part milling. CIRP Ann-Manuf. Technol. 2020;69:313-316.

[58] Kiss KA, Bachrathy D, Stépán G. Cumulative surface location error for milling processes based on tool-tip frequency response function. Procedia CIRP, 2016;46:323-326.

[59] Schmitz TL, Honeycutt A, Gomez M, Stokes M, Betters E. Multi-point coupling for tool point receptance prediction J. Manuf. Process. 2019;43:2-11.

[60] Wiercigroch M, Budak E. Sources of nonlinearities, chatter generation and suppression in metal cutting. Philos. Trans. R. Soc. A-Math. Phys. Eng. Sci. 2001;359:663-693.

[61] Rusinek R, Wiercigroch M, Wahi P. Modelling of frictional chatter in metal cutting. Int J Mech Sci. 2014;89:167-176.

[62] Yan Y, Xu J, Wiercigroch M, Guo Q. Statistical basin of attraction in time-delayed cutting dynamics: Modelling and computation. Physica D. 2021;416:132779.

[63] Ji YL, Bi QZ, Yu L, Ren F, Wang YH. A robust RCSA-Based method for the in situ measurement of rotating tool-tip frequency response functions. J. Manuf. Sci. Eng 2020;142:081004-1-081004-11.

[64] Schmitz TL, Honeycutt A, Gomez M, Stokes M, Betters E. Multi-point coupling for tool point receptance prediction J. Manuf. Process 2019;43:2-11.

[65] Wang DQ, Löser M, Luo YH, Ihlenfeldt S, Wang XB, Liu ZB. Prediction of cumulative surface location error at the contact zone of in-process workpiece and milling tool. Int J Mech Sci. 2020;177:105543.

[66] Wang DQ, Löser M, Ihlenfeldt S, Wang XB, Liu ZB. Milling stability analysis with considering process damping and mode shapes of in-process thin-walled workpiece. Int J Mech Sci. 2019;159:382-397.

[67] Rubeo MA, Schmitz TL. Mechanistic force model coefficients A comparison of linear regression and nonlinear optimization. Precis. Eng 2016;45:311-321.

[68] Yan ZH, Wang XB, Liu ZB, Wang DQ, Jiao L, Ji YJ. Third-order updated full discretization method for milling stability prediction. Int J Adv Manuf Technol. 2017;92:2299-2309.

[69] Özgüven HN. Structural modifications using frequency response functions. Mech Syst Signal Process. 1990;4(1):53–63.

[70] Sestieri, A. Structural dynamic modification. Sadhana. 2000;25:247–259.

[71] Wan M, Ma YC, Zhang WH, Yang Y. Study on the construction mechanism of stability lobes in milling process with multiple modes. Int J Adv Manuf Technol. 2015;79:589-603.

[72] Hutchinson JR. Shear coefficients for Timoshenko beam theory. J. Appl. Mech 2001;68:87-92.

[73] Qi B, Sun YW, Li ZY Tool point frequency response function prediction using RCSA based on Timoshenko beam model. Int J Adv Manuf Technol 2017;92:2787-2799.

Appendix A: Receptance coupling for Timoshenko beam model

When the axial effects are not considered, the Timoshenko beam model can be described by the linear partial differential equations:

$$\begin{cases} \rho A \dfrac{\partial^2 y}{\partial t^2} = \dfrac{\partial}{\partial x}\left[\kappa A G\left(\dfrac{\partial y}{\partial x} - \varphi\right)\right], \\ \rho I \dfrac{\partial^2 \varphi}{\partial t^2} = \dfrac{\partial}{\partial x}\left(EI\dfrac{\partial \varphi}{\partial x}\right) + \kappa A G\left(\dfrac{\partial y}{\partial x} - \varphi\right), \end{cases} \tag{A-1}$$

where ρ is the density, A is the cross-section area, E is the elastic modulus, G is the shear modulus, I is the area moment of inertia, κ is the Timoshenko shear coefficient [72], and φ is the angular displacement. Based on Eq. (A-1), the differential equation describing the Timoshenko beam model can be further expressed as:

$$EI\frac{\partial^4 y}{\partial x^4} + \rho A \frac{\partial^2 y}{\partial t^2} - \rho I\left(1 + \frac{E}{kG}\right)\frac{\partial^4 y}{\partial x^2 \partial t^2} + \frac{\rho^2 I}{kG}\frac{\partial^4 y}{\partial t^4} = 0. \tag{A-2}$$

After the trial function, $y = Y(x)\sin(\omega t)$, is applied to eliminate the time dependence, Eq. (A-2) becomes:

$$\frac{\partial^4 Y}{\partial x^4} + \tau_1 \frac{\partial^2 Y}{\partial x^2} + \tau_2 Y = 0, \tag{A-3}$$

where $\begin{cases} \tau_1 = \rho\omega^2\left(\dfrac{1}{E} + \dfrac{1}{kG}\right) > 0, \\ \tau_2 = \dfrac{\rho^2\omega^4}{EkG} - \dfrac{\rho A\omega^2}{EI} < 0, \end{cases}$ and ω is angular frequency.

The eigen solution to Eq. (A-3) can be written as:

$$\begin{cases} \left(\lambda^2 + \dfrac{\tau_1}{2}\right)^2 = \dfrac{\tau_1^2}{4} - \tau_2, \\ \dfrac{\tau_1^2}{4} - \tau_2 > 0, \end{cases} \tag{A-4}$$

where $\begin{cases} m = \sqrt{\dfrac{\tau_1}{2} + \sqrt{\dfrac{\tau_1^2}{4} - \tau_2}}, \\ n = \sqrt{-\dfrac{\tau_1}{2} + \sqrt{\dfrac{\tau_1^2}{4} - \tau_2}}. \end{cases}$

The general solution to Eq. (A-2) can be developed as:

$$Y = A_1\cos(mx) + B_1\sin(mx) + C_1\cosh(nx) + D_1\sinh(nx), \tag{A-5}$$

where A_1, B_1, C_1 and D_1 are the constants for different initial boundary conditions.

For the clamped-free beam model, the constants satisfy:

$$\begin{cases} A_1 = -C_1, \\ B_1 = -\dfrac{n}{m}D_1. \end{cases} \tag{A-6}$$

When harmonic force $F\sin(\omega t)$ is applied:

$$
\begin{cases}
C_1 = \dfrac{F\sin(\omega t)[mn\sin(mL)+n^2\sinh(nL)]}{EI[m^4 n + n^5 + 2m^2 n^3 \cos(mL)\cosh(nL) + (m^3 n^2 - mn^4)\sin(mL)\sinh(nL)]}, \\[2mm]
D_1 = \dfrac{-F\sin(\omega t)[m^2\cos(mL)+n^2\cosh(nL)]}{EI[m^4 n + n^5 + 2m^2 n^3 \cos(mL)\cosh(nL) + (m^3 n^2 - mn^4)\sin(mL)\sinh(nL)]},
\end{cases}
\tag{A-7}
$$

where L is the length of the beam in Eq. (A-5), i.e., $x = L$.

When harmonic bending couple $M\sin(\omega t)$ is applied:

$$
\begin{cases}
C_1 = \dfrac{M\sin(\omega t)[m^2 n\cos(mL)+n^3\cosh(nL)]}{EI[m^4 n + n^5 + 2m^2 n^3 \cos(mL)\cosh(nL) + (m^3 n^2 - mn^4)\sin(mL)\sinh(nL)]}, \\[2mm]
D_1 = \dfrac{M\sin(\omega t)[m^3\sin(mL)-n^3\sinh(nL)]}{EI[m^4 n + n^5 + 2m^2 n^3 \cos(mL)\cosh(nL) + (m^3 n^2 - mn^4)\sin(mL)\sinh(nL)]}.
\end{cases}
\tag{A-8}
$$

For the free-free beam model, the constants satisfy:

$$
\begin{cases}
A_1 = \dfrac{n^2}{m^2} C_1, \\[2mm]
B_1 = \dfrac{n^3}{m^3} D_1.
\end{cases}
\tag{A-9}
$$

When harmonic force $F\sin(\omega t)$ is applied, we obtain:

$$
\begin{cases}
C_1 = \dfrac{F\sin(\omega t)\left[-\dfrac{n^3}{m}\sin(mL)+n^2\sinh(nL)\right]}{EI\left[2n^5 - 2n^5\cos(mL)\cosh(nL) + \left(\dfrac{n^6}{m}-mn^4\right)\sin(mL)\sinh(nL)\right]}, \\[4mm]
D_1 = \dfrac{F\sin(\omega t)[n^2\cos(mL)-n^2\cosh(nL)]}{EI\left[2n^5 - 2n^5\cos(mL)\cosh(nL) + \left(\dfrac{n^6}{m}-mn^4\right)\sin(mL)\sinh(nL)\right]}.
\end{cases}
\tag{A-10}
$$

When harmonic bending couple $M\sin(\omega t)$ is applied:

$$
\begin{cases}
C_1 = \dfrac{M\sin(\omega t)[-n^3\cos(mL)+n^3\cosh(nL)]}{EI\left[2n^5 - 2n^5\cos(mL)\cosh(nL) + \left(\dfrac{n^6}{m}-mn^4\right)\sin(mL)\sinh(nL)\right]}, \\[4mm]
D_1 = \dfrac{M\sin(\omega t)[-mn^2\sin(mL)-n^3\sinh(nL)]}{EI\left[2n^5 - 2n^5\cos(mL)\cosh(nL) + \left(\dfrac{n^6}{m}-mn^4\right)\sin(mL)\sinh(nL)\right]}.
\end{cases}
\tag{A-11}
$$

According to the boundary conditions of the beam, the receptance can be obtained with clamped-free mode and free-free mode. Since Timoshenko beam model considers the shear effects, N_{uv} and P_{uv}, Eq. (1) cannot be directly achieved by deriving from Eq. (A-5). Instead, the rotation angle is developed by iteration [73].

$$
\varphi_i = \varphi_{i-1} + \left(\frac{\rho I \omega^2}{kAG}\right)^{i-1}\varphi_{i-1},\ (i > 1).
\tag{A-12}
$$

Thus, Eq. (1) can be redefined as:

$$
R_{uv} = \begin{pmatrix}
\dfrac{Y_u}{f_v} = H_{uv}, & \dfrac{Y_u}{\chi_v} = L_{uv} \\[3mm]
\dfrac{\varphi_u}{f_v} = N_{uv}, & \dfrac{\varphi_u}{\chi_v} = P_{uv}
\end{pmatrix}.
\tag{A-13}
$$
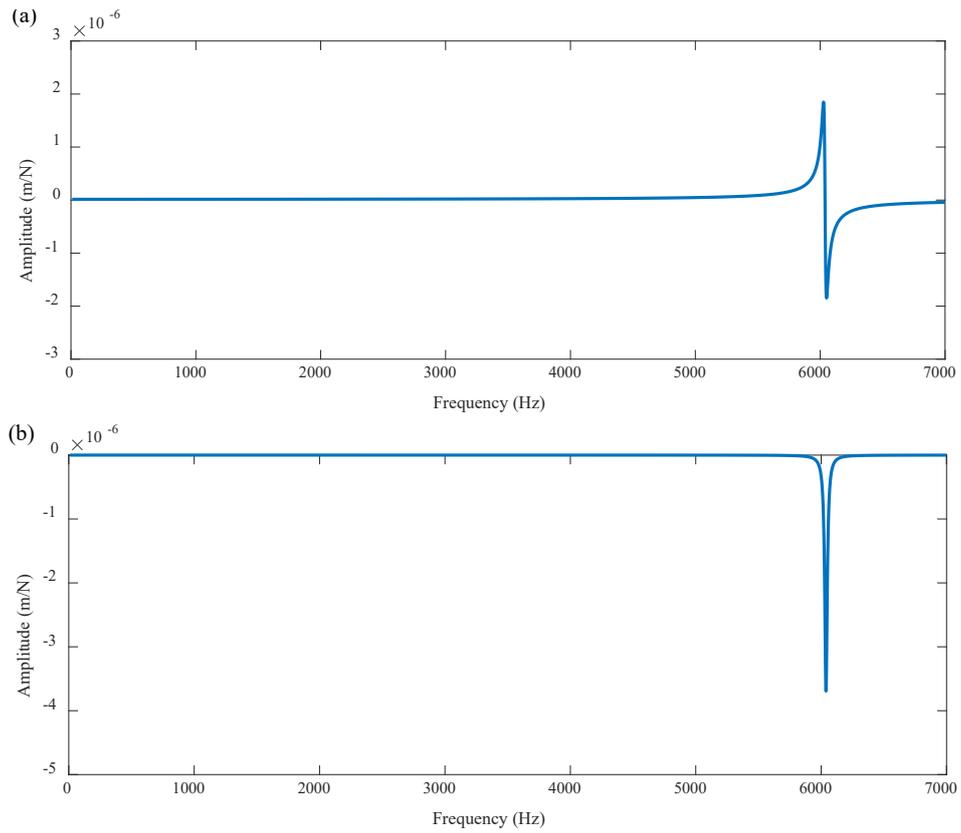
Figure A-1. FRF prediction of workpiece at Stage 1 with Timoshenko beam model; (a) real part of the FRF in rigid coupling state; (b) imaginary part of the FRF in rigid coupling state.